論文 / 著書情報
Article / Book Information

題目(和文)	ユウロピウム原子のボース・アインシュタイン凝縮
Title(English)	Bose-Einstein condensate of europium atoms
著者(和文)	宮澤裕貴
Author(English)	Yuuki Miyazawa
出典(和文)	学位:博士(理学), 学位授与機関:東京工業大学, 報告番号:甲第12053号, 授与年月日:2021年9月24日, 学位の種別:課程博士, 審査員:上妻 幹旺,藤澤 利正,金森 英人,西田 祐介,相川 清隆
Citation(English)	Degree:Doctor (Science), Conferring organization: Tokyo Institute of Technology, Report number:甲第12053号, Conferred date:2021/9/24, Degree Type:Course doctor, Examiner:,,,,
学位種別(和文)	博士論文
Type(English)	Doctoral Thesis

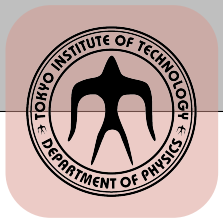

Tokyo Institute of Technology
School of Science
Department of Physics

Bose-Einstein condensate of europium atoms

PhD Thesis

YUKI MIYAZAWA

Supervisor: Mikio Kozuma
Professor

Tokyo, October 2021

Abstract

Ultracold atoms with a large magnetic moment interact with each other with long-range and anisotropic magnetic dipole-dipole interaction. Therefore, the nature is expected to be significantly different from that of other ultracold atoms. In recent years, strongly dipolar atomic species of Cr, Dy, and Er have been brought to quantum degeneracy and rich dipolar phenomena have been observed such as d-wave collapse, deformation of the Fermi surface, and Rosensweig instability, quantum droplets, and dipolar supersolid. Considering such results, I focused on the europium atom (Eu), which has a large dipole moment. Unlike other dipolar atoms such as Cr, Dy, and Er, Eu has stable bosonic isotopes with hyperfine structures. Therefore, the s-wave scattering length of bosonic Eu can be controlled with maintaining spin degrees of freedom. Bose-Einstein condensate with magnetic dipole interaction and spin degree of freedom is expected to show rich quantum phases where spin angular momentum and orbital angular momentum couple each other. Europium is a good candidate to search such quantum phases systematically.

In this thesis, I report on the first realization of Bose-Einstein condensate of europium atoms. This thesis in particular describes how to cool Eu atoms. Due to the complex energy structure of the Eu atom, the standard laser cooling method cannot be applied to create a Eu BEC. It is revealed in my master course study that the only $J \to J+1$ strong transition has large optical leaks to six metastable states with a probability of 10^{-3}. This value is too high to slow down the Eu atomic beam, which makes it difficult to laser cool Eu. Considering the result, I optically pump atoms to $a^{10}\mathrm{D}_{13/2}$ metastable state and implemented Zeeman slowing and magneto-optical trapping with a quasi-cyclic transition at a wavelength of 583 nm and nurtural linewidth of 8.2 MHz.

The starting point of this thesis is the metastable magneto-optical trap of europium mentioned above. Since the metastable state is not stable enough to produce a BEC, I optically pumped back the trapped cold metastable atoms to the ground state and captured them in a magneto-optical trap operating with a transition at a wavelength of 687 nm and a natural linewidth of 97 kHz. Although this transition has large optical leaks to three metastable states, I plugged the leaks by repumping atoms from the metastable state to the ground state with three color infrared laser lights. In this way, I successfully trap 4.7×10^7 ^{151}Eu atoms in the ground state. Thanks to the narrow natural linewidth of the cooling transition, the temperature reached to 6 μK, which is a good starting condition for direct loading to an optical dipole trap. In addition, we measured the optical leak probabilities from the excited state to the metastable state, which was estimated to be 2.7×10^{-2} in total.

Then we loaded the cold atoms to an optical dipole trap operating at a wavelength of 1550 nm for evaporative cooling, resulting in almost pure condensates of ^{151}Eu with 1.5×10^4 atoms. The effect of dipole-dipole interaction of the BEC was observed as the deformation of the expanding Eu condensate; the shape of the BEC after free expansion strongly depends on the orientation of the atomic dipole moments. By comparing the deformation of the condensate to the numerical simulation, I extracted an s-wave scattering length of $a_s = 135\, a_B$. In addition, I found a Feshbach resonance at a magnetic field of

1.3 G, and the shape of the condensate deformed in the vicinity of the resonance, which suggests a change of the s-wave scattering length.

This study paves the way for quantum simulation using a strongly dipolar BEC. The unique properties of Eu BEC might open new directions of investigation in the field of strongly dipolar quantum gases.

Contents

List of Figures

List of Tables

1.1 Ultracold atoms

Ultracold atoms are gaseous atoms that are trapped in a vacuum chamber at a temperature close to 0 kelvin (typically below a few μK). At these temperatures, the thermal de Broglie wavelength of the atoms reaches interatomic distance and quantum mechanical properties become important. One of the famous phenomena is Bose-Einstein condensate (BEC), where the large fraction of bosons occupy the lowest quantum state, which was first observed in 1995 by using rubidium atoms [1] and sodium atoms [2].

1.2 Historical background of dipolar quantum gases

Interaction of conventional ultracold atoms is characterized by s-wave scattering length a_s, and its interaction potential is written as:

$$U_{contact}(r) = \frac{4\pi\hbar^2 a_s}{m}\delta(r) \tag{1.1}$$

where m is the atomic mass. The interaction has short-range and isotropic character.

On the other hand, in the case of atoms with magnetic dipole moment, atoms interact via dipole dipole interaction (DDI), whose interaction potential is

$$U_{dd}(\vec{r}) = \frac{\mu_0}{4\pi r^3}\left((\vec{\mu_1}\cdot\vec{\mu_2}) - \frac{3}{r^2}(\vec{\mu_1}\cdot\vec{r})(\vec{\mu_2}\cdot\vec{r})\right) \tag{1.2}$$

where $\vec{\mu_1}$ and $\vec{\mu_2}$ is the magnetic dipole momenta of two atoms, $\vec{r}$ is the relative position vector. The interaction has a long-range and anisotropic character, which is completely different from the s-wave contact interaction. By introducing the DDI to the ultracold atom system, many fascinating phenomena were theoretically predicted and some of them were experimentally demonstrated. I will show some examples in the following three systems.

1.2.1 Dipolar effects in polarized dipolar BEC

Here we assume that all atoms are in the lowest Zeeman level under a static magnetic field. The system is characterized by the relative strength of DDI against s-wave contact interaction

$$\epsilon_{dd} = \frac{\mu_0\mu_m^2 m}{12\pi\hbar^2 a_s} \tag{1.3}$$

where μ_m is the magnetic dipole moment of the atom. The ϵ_{dd} for some atoms are listed in Table 1.1. If the ϵ_{dd} is much smaller than 1, DDI affects little the BEC system, which is in the case of alkali metal atoms.

In 2005, the BEC of chromium (Cr) atom was realized [7] by the group of Tilman Pfau. Since the Cr atom has a large dipole moment of $6\,\mu_B$, their DDI is 36 times larger than alkali atoms. The large DDI results in $\epsilon_{dd} = 0.15$ and affects the shape of the BEC, which was first observed in 2007 [8]. The shape of the BEC after free expansion was slightly

Species	$\mu_m\,(\mu_B)$	$a_s\,(a_B)$	ϵ_{dd}	Ref.
^{87}Rb	1	95	0.007	[3]
^{52}Cr	6	103	0.15	[4]
^{166}Er	6.98	72	0.91	[5]
^{164}Dy	9.93	92	1.44	[6]
^{151}Eu	6.98	?	?	

Table 1.1: Dipole moment μ_m, s-wave scattering length a_s, and relative strength of DDI ϵ_{dd}. The s-wave scattering length of ^{151}Eu is not known.

elongated by DDI along the direction of the atomic dipole. In addition, $\epsilon_{dd} > 1$ regime was realized by reducing s-wave scattering length by using Feshbach resonance. In such a regime, the system becomes unstable due to the attractive interaction of the DDI. They observed the d-wave symmetric collapse of Cr BEC by tuning s-wave scattering length with a Feshbach resonance [9].

After several years later, more magnetic atoms of erbium (Er) and dysprosium (Dy), which belong to lanthanide seriese, were laser-cooled and brought to quantum degeneracy [10, 11]. Their incomplete electronic ^4f-shells provide large magnetic dipole moment. Thanks to the combination of the large dipole moment and large atomic mass, they have one order of magnitude larger ϵ_{dd} than Cr, which are listed in Table 1.1. By using these strongly dipolar atoms, new quantum phase, named quantum droplet, was successfully observed [12, 13]. Although ϵ_{dd} was tuned larger than 1 by Feshbach resonance, the quantum fluctuation stabilizes BEC against collapse and the quantum gas acts as a liquid-like self bound droplet. In addition, by precisely investigating the system, phase coherence in droplet arrays was observed [14], which indicates the emergence of the supersolid phase. The supersolid phase has both the crystalline structure of a solid and the frictionless flow of a superfluid, which was initially investigated in liquid helium system and has not been observed yet [15]. The supersolid phase is currently being investigated eagerly [16].

Polarized dipolar BEC is a current hot research field.

1.2.2 Dipolar effects in spinor BEC

Another interesting dipolar system is a spinor BEC with DDI (spinor dipolar BEC). Many fascinating ground-state properties and spin dynamics of spinor dipolar BEC were theoretically predicted [17–19] under ultra-low magnetic field, where the Zeeman energy is lower than DDI energy (magnetic field of typically $10 \sim 100\,\mu$G).

Here we start the explanation of spinor BEC. A spinor BEC is a BEC with spin internal degrees of freedom. It was first realized with spin-1 sodium BEC confined in an optical dipole trap [20]. The interaction of a spinor BEC is characterized by spin-independent s-wave scattering interaction and spin-dependent s-wave scattering interaction. In the case of spin-1 BEC, spin-independent s-wave scattering interaction is written as [17]

$$U_0(r) = \frac{4\pi\hbar^2(a_0 + 2a_2)}{3m}\delta(r) \tag{1.4}$$

and spin-dependent s-wave scattering interaction is written as

$$U_1(r) = \frac{4\pi\hbar^2(a_2 - a_0)}{3m}\delta(r) \tag{1.5}$$

where a_s $(s = 0, 2)$ is the s-wave scattering length for the scattering channel with total spin s. If the spin-dependent interaction is negative, the spinor BEC prefers ferromagnetic phase, whereas if the spin-dependent interaction is positive, the spinor BEC prefers polar phase [21].

In addition to the s-wave spin dependent/independent interaction, a spinor dipolar BEC interacts with DDI. Since the DDI couples atomic spin and orbital angular momentum, the system of spinor BEC would be drastically changed by DDI. Spin texture of the spinor dipolar BEC will be created by the competition between spin-dependent interaction and DDI. Kawaguchi predicted that the spin-1 ferromagnetic Bose-Einstein condensate with DDI has three ground state phases: polar-core vortex (PCV) phase, flower (FL) phase, and chiral spin-vortex (CSV) phase [17] and also predicted that it is observable with spin-1 ^{87}Rb BEC. These ground state phases in spinor dipolar BEC exhibit spin texture and spontaneous mass current circulation.

However, these quantum phases have not been realized experimentally since there is some technical difficulties to produce such quantum phases. To form such a spin texture in the ground state, the Zeeman energy must be smaller than the dipolar interaction energy. Since DDI of the spin-1 ^{87}Rb is quit small ($\sim$ sub nK), the stray magnetic field must be smaller than 10 μG [17]. It hinders the experimental realization of these quantum ground phases.

A spin-3 ^{52}Cr BEC seems to be one of the good candidate to explore these spinor dipolar BEC system since Cr has large dipole moment of 6 μ_B. The large dipole moment increases DDI energy about one order of magnitude compared to spin-1 ^{87}Rb and relaxes restrictions on the stray magnetic field. However, since spin-dependent interaction of Cr is much larger than DDI, observable DDI effect of ^{52}Cr spinor dipolar BEC would be limited [22]. [1]

Note that such a ground state phases have not been realized yet, DDI effects in spinor dipolar BEC under static magnetic field were successfully observed. Larmor precession of spinor dipolar BEC under static magnetic field were modified by DDI [23–26]. The observed spin dynamics of the Larmor precessions were well described by the numerical calculations.

1.2.3 Dipolar atoms in an optical lattice

Dipolar atoms in an optical lattice is also interesting. By preparing Er atoms in a 3D optical lattice, extended Bose-Hubbard model was realized [27]. Controlling the orientation of the atomic dipoles, they revealed the anisotropic character of the onsite interaction and hopping dynamics, and their influence on the superfluid-to-Mott insulator quantum phase transition.

[1] Note that spin-dependent interactions of Er and Dy are not known.

By preparing Cr atoms in tightly confined 3D optical lattice, spin dynamics of atoms in the optical lattice was investigated [28].

1.3 Purpose of this thesis

The purpose of this thesis is to realize a Bose-Einstein condensate (BEC) of Eu atoms, which has also large magnetic moment of $7\mu_B$. Since Eu has unique properties: hyperfine structure and highly symmetric electronic ground state, Eu atoms may have some advantage for investigating dipolar bosonic quantum gases.

In particular, I am focused on the hyperfine structure in the ground state. Since Eu has bosonic isotopes that have hyperfine structure in their ground states, microwave-induced Feshbach resonance is in principle applicable [29]. In contrast to conventional magnetic-field-induced Feshbach resonance, microwave-induced Feshbach resonance can be used under zero magnetic field since open channel is coupled to a bound state by microwave (Fig. 1.1). It is a great advantage for exploring ground state phases of the spinor dipolar BEC. As if spin-dependent s-wave scattering interaction of Eu was large like ^{52}Cr, one would suppress the spin-dependent interaction with the microwave-induced Feshbach resonance. In addition, fine tuning of the s-wave scattering length enable us to investigate these ground state phases in details.

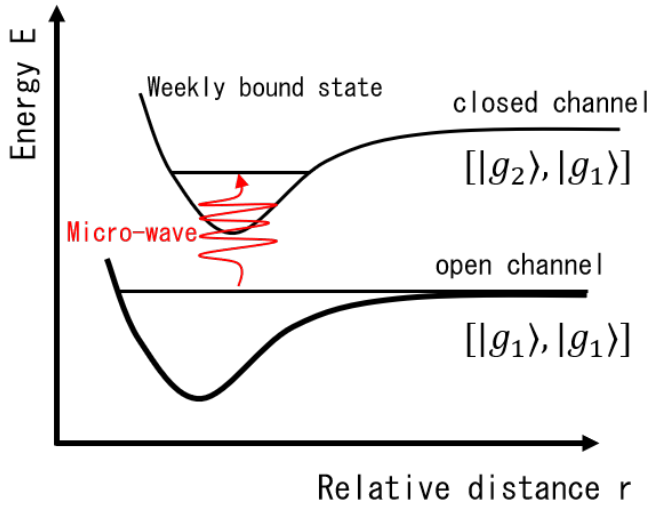

Figure 1.1: Scheme of microwave-induced Feshbach resonance. $|g_1\rangle$ and $|g_2\rangle$ indicate internal states of atoms.

I also note that the large dipole moment of Eu is preferable for the microwave-induced Feshbach resonance. The scattering length as a function of the microwave frequency ω is written as [29]

$$a(\omega) = a_{bg}\left(1 + \frac{\Delta\omega}{\omega - \omega_{res}}\right) \tag{1.6}$$

where a_{bg} is the background scattering length, which is the scattering length without microwave, ω_{res} is the resonant frequency, and $\Delta\omega$ is the width of the Feshbach resonance. Precise control of the scattering length requires larger $\Delta\omega$, which is proportional to the

overlap integral of the open and closed channel wave functions, called Franck–Condon factor, and the square of magnetic dipole interaction between the atoms and the microwave. The $\Delta\omega$ for alkali atoms with the oscillating magnetic field amplitude of $B_0 = 1\,\mathrm{G}$ are calculated to be $6 \sim 4500\,\mathrm{Hz}$ in Ref. [29]. Some atoms have small $\Delta\omega$ due to small Franck-Condon factors. On the other hand, since Eu has large dipole moment of $7\,\mu_B$, $\Delta\omega$ of Eu will be increased by 49 times than those of alkali atoms. Although the Franck–Condon factor for Eu is not known, large $\Delta\omega$ can be expected.

1.4 Thesis overview

This thesis is organized as follows:

Chapter 2: Europium properties

A brief description of the properties of Eu atoms.

Chapter 3: Strategy for laser cooling of europium

Due to complex energy structure of Eu, standard laser cooling method cannot be applied. In this chapter, we briefly explain our previous work on laser cooling of Eu. Then, based on the results, I suggest a new strategy for laser cooling of Eu, which is demonstrated in chapter 5.

Chapter 4: Experimetal setup

In this chapter, I describe experimental setup, which contains vacuum apparatus and laser systems.

Chapter 5: Narrow-line magneto-optical trapping for europium

Base on the strategy described in chapter 3, I realized first laser cooling of Eu in the ground state by using a narrow-line magneto optical trapping. This chapter describes the features of the magneto-optical trap including number of atoms, loss rate, spin polarization and temperature.

Chapter 6: Optical dipole trap for europium

Cold atoms trapped in the narrow-line magneto optical trap are loaded to an optical dipole trap for further cooling. This chapter describes the loading process and the dynamic polarizability of Eu.

Chapter 7: Bose-Einstein condensate for europipum

Through evaporative cooling in an optical dipole trap we create a Eu BEC. This chapter described evidence of the phase transition to BEC. In addition, some characters of the BEC are presented.

1.5 List of publications

Chapter 3 and 5 of this thesis have been summarized in the following journal articles:

- Yuki Miyazawa, Ryotaro Inoue, Keiji Nishida, Toshiyuki Hosoya, and Mikio Kozuma, *Measuring the branching ratios from the $y^8P_{9/2}$ state to metastable states in europium*, Opt. Commun. **392**, 171 (2017).
- Ryotaro Inoue, Yuki Miyazawa, and Mikio Kozuma, *Magneto-optical trapping of optically pumped metastable europium*, Physical Review A **97**, 061607(R) (2018)
- Yuki Miyazawa, Ryotaro Inoue, Hiroki Matsui, Kenta Takanashi, and Mikio Kozuma, *Narrow-line magneto-optical trap for europium*, Physical Review A **103**, 053122 (2021)

Chapter 2: Europium properties

Europium (Eu) is a rare-earth metal belonging to the lanthanide series of the periodic table and named after the continent of Europe. In this chapter, I introduce the properties of Europium.

2.1 Electron configuration and term

Electron configuration and term of Eu is

$$[Xe]\,4f^7 6s^2 \quad a^8\mathrm{S}_{7/2} \tag{2.1}$$

Since Eu has half-filled $4f$ valence electron within a filled $6s$ shell, the orbital angular momentum is zero, whereas magnetic dipole moment is as large as $7\,\mu_B$, which stems form aligned $4f$ electronic spin. The large dipole moment enables us to investigate dipolar bosonic quantum gases described in Sec. 1.2.

In addition, the zero-electronic-orbital ground state is in contrast to the other dipolar lanthanides, whose large electronic orbital provides a strong anisotropy and the resultant rich scattering behavior [30–33]. As with the case of conventional ultracold alkaline atoms, a scattering length of Eu is expected to be well controlled by using magnetic-field induced Feshbach resonance [34].

2.2 Stable isotopes

Europium has two stable isotopes of ^{151}Eu and ^{153}Eu, which are listed in Table 2.1. Both isotopes are boson and have nuclear spin of $I = 5/2$. The interaction of the nuclear spin with the magnetic field generated by th electrons induces hyperfine splittings.

isotope	isotopic mass [35]	abundance [35]	half-life [36]	nuclear spin [37]	statistics
^{151}Eu	150.919846(3)	47.81(6) %	4.6×10^{18} y	5/2	boson
^{153}Eu	152.921227(3)	52.19(6) %	-	5/2	boson

Table 2.1: Stable isotopes of Eu

2.3 Hyperfine structure in the ground state

The hyperfine structure of ^{151}Eu and ^{153}Eu is shown in Fig. 2.1. The hyperfine splitting is calculated by hyperfine splitting constant A and B in Ref. [38].

The hyperfine structure may be advantage for investigating spinor dipolar BEC. The s-wave scattering length can in principle be controlled by using the microwave-induced Feshbach resonance [29,39] even under zero magnetic field. In addition, hyperfine splitting of ∼100 MHz order is preferable for microwave-induced Feshbach resonance since one may

induce a Feschbach resonance in a near field region, i.e. one could create the vibrating magnetic field with a simple loop antenna.

Note that the bosonic isotopes of Cr, Dy, and Er do not have hyperfine structures in their ground states. Holmium (Ho), which has already been laser-cooled [40], is one of the good candidates since it has large dipole moment (9 μ_B) and a stable bosonic isotope (^{165}Ho) with non-zero nuclear spin. However, there is a concern about the inelastic loss due to hyperfine exchanging collision [41] in the investigation of the ground-state phases using ultracold Ho atoms, since its hyperfine state with maximum magnetic moment does not correspond to the lowest energy one in contrast to the case of Eu (see Fig. 2.1).

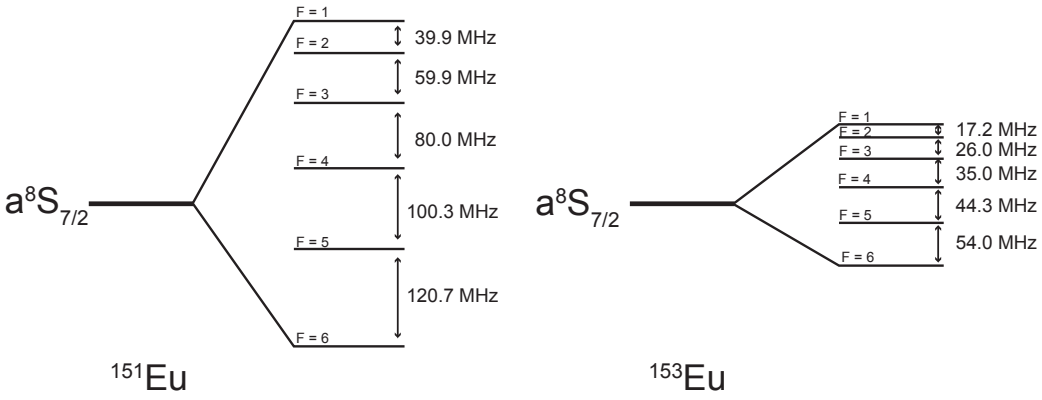

Figure 2.1: Hyperfine structure of Eu in the ground state.

2.4 Physical properties

Physical properties of Eu are listed in Table 2.2. Europium is in solid state at a room temperature and has high melting and boiling point. Since Eu is the most reactive rare-earth element, it rapidly oxidizes in air and gets yellow. Thus, one have to be careful, dealing with europium metal.

atomic number	atomic mass	density	melting point	boiling point
63	151.965 amu	5.244 g/cm^3	822 °C	1527 °C

Table 2.2: Physical property of Eu [42]

2.5 Saturated vapor pressure

Saturated vapor pressures of elements are generally described as

$$\log_{10} p\,(atm) = A + B \cdot T^{-1} + C \log_{10} T + D \cdot T \cdot 10^{-3} \tag{2.2}$$

where A, B, C and D are constants and T is the temperature [K] [43]. These constants for solid Eu is known and listed in Table 2.3. Figure 2.2 shows the saturated vapor pressure curve calculated based on Eq.2.2 with the constants. Our atomic oven described in Sec. 4.1.1 operates at 500°.

Element	state	A	B	C	D	temperature range [K]
Eu	solid	6.479	-9340	-0.1659	-0.3600	298 - melting point

Table 2.3: Constants of saturated vapor pressure of Eu [43]

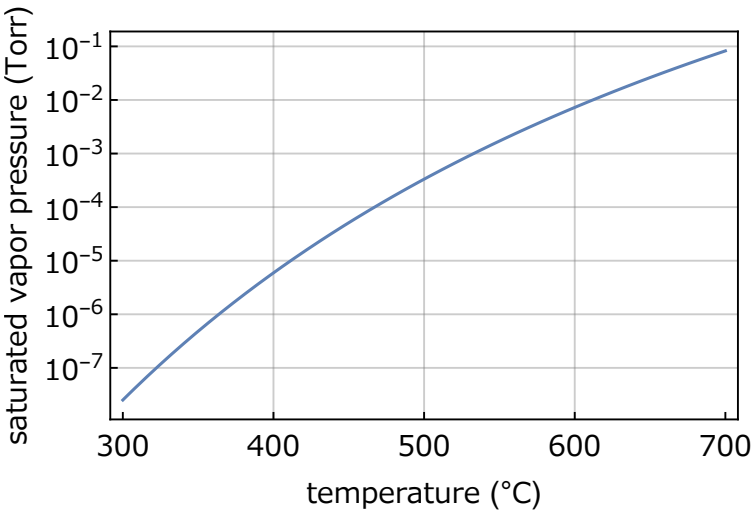

Figure 2.2: Saturated vapor pressure of Eu

Chapter 3: Strategy for laser cooling of europium

Laser cooling and trapping is a very powerful tool to produce a cold sample of neutral atoms or molecules. It is a fundamental technique to create a BEC. However, europium has complex level structure that makes laser cooling more difficult than other species. In our early works, we investigated the feasibility of the laser cooling using $a^8\mathrm{S}_{7/2} - y^8\mathrm{P}_{9/2}$ transition and concluded that Zeeman slowing using this transition is problematic [44]. Reflecting the result, we optically pumped the atoms from the ground state to metastable state and laser cool the metastable europium atoms using $a^{10}\mathrm{D}_{13/2} - z^{10}\mathrm{F}_{15/2}$ transition [45]. In this chapter, I describe short summaries of these early works and discuss the strategy for laser cooling of europium in the ground state.

3.1 Branching ratios from the $y^8\mathrm{P}_{9/2}$ state to metastable states

3.1.1 Laser cooling transitions for europium

Figure 3.1 shows energy levels of europium below 25000 cm^{-1}. The ground state of europium is in $4f^7 6s^2\ a^8\mathrm{S}^\circ_{7/2}$ configuration. To laser-cool europium atoms, we need a transition from the ground state with $J \to J+1$ change in electric angular momentum, which can be used for Zeeman slowing or magneto-optical trapping (MOT). Figure 3.1 also shows the possible $J \to J+1$ transitions from the ground state, whose parameters are listed in Table 3.1. One supposes that the 460-nm broad transition is suitable for efficient Zeeman slowing, whereas the 687-nm narrow transition is better for MOT to achieve lower temperature. The combination of Zeeman slowing using a broad optical transition and MOT with a narrow optical transition was successfully conducted in other lanthanide atoms, such as Yb [46], Dy [47], Er [48], and Tm [49]. However, this approach cannot be applied for Eu due to the optical leak problem, which is described in detail in the following paragraph.

		$a^8\mathrm{S}_{7/2} - y^8\mathrm{P}_{9/2}$	$a^8\mathrm{S}_{7/2} - z^8\mathrm{P}_{9/2}$	$a^8\mathrm{S}_{7/2} - z^{10}\mathrm{P}_{9/2}$	ref
Wavelength	λ	460 nm	602 nm	687 nm	
Natural linewidth	$\Gamma/2\pi$	26 MHz	150 kHz	97 kHz	
Doppler temperature	T_D	360 μK	3.6 μK	2.3 μK	
Saturation intensity	I_{sat}	35 mW/cm^2	90 μW/cm^2	40 μW/cm^2	
Recoil velocity	v_{recoil}	5.8 mm/s	4.4 mm/s	3.8 mm/s	
Wave number	$1/\lambda$	21761.26 cm^{-1}	16611.79 cm^{-1}	14563.57 cm^{-1}	[50]
Lifetime	τ	6.1(3) ns [a]	1060(60) ns [b]	1635(80) ns [b]	[a] [51] [b] [52]

Table 3.1: $J \to J+1$ transitions for europium in the ground state.

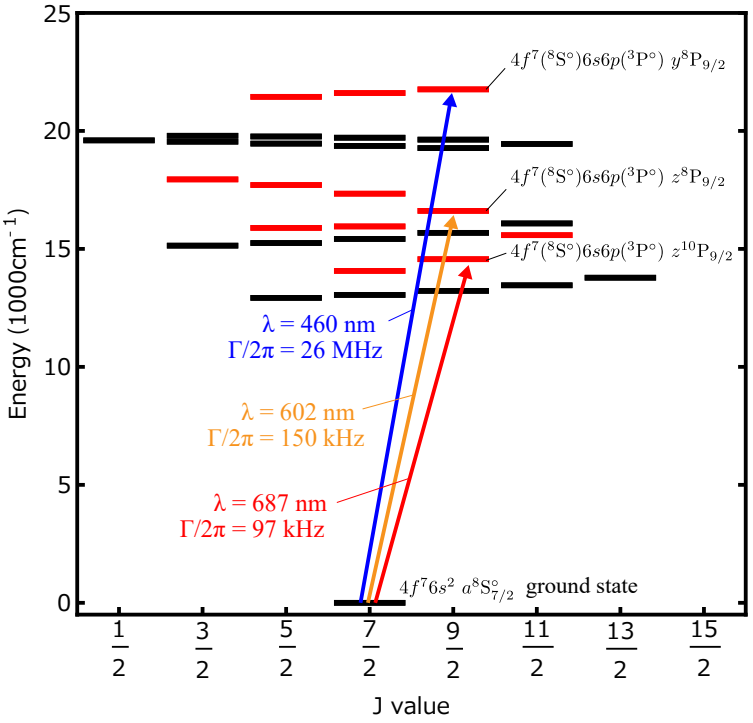

Figure 3.1: Energy levels of europium below 25000 cm^{-1} [50], showing $J \rightarrow J+1$ transitions from the ground state. Red (black) horizontal lines indicate even (odd) parity states.

3.1.2 Branching ratios from the $y^8P_{9/2}$ to metastable states

The 460-nm transition is the only feasible candidate to decelerate an atomic beam. However, atoms in $y^8P_{9/2}$ excited state can decay to eleven metastable states through electric-dipole transitions, which is shown in Fig. 3.2. High probability that atoms decay to these metastable states makes the Zeeman slowing inefficient since atoms in these metastable states cannnot interact with the 460-nm light. Among the eleven transitions, we measured branching ratios for three intercombination transitions ($y^8P_{9/2} - a^{10}D_{7/2,\ 9/2,\ 11/2}$, wavelength: 1148 $\sim$ 1204 nm) and three allowed ones ($y^8P_{9/2} - a^8D_{7/2,\ 9/2,\ 11/2}$, wavelength: 1577 $\sim$ 1760 nm) through fluorescence spectroscopy of an atomic beam [44]. The result is summarized in Table 3.2. The sum of the six branching ratios is up to $1.05(2) \times 10^{-3}$, which is two orders of magnitude larger than the optical leak probabilities reported in other lanthanide experiments [53–56].

3.1.3 Feasibility of Zeeman slowing using the 460-nm transition

Here, I discuss the feasibility of Zeeman slowing using the 460-nm transition based on the result of the branching ratio measurement. The efficiency of the Zeeman slowing can be estimated by comparing the optical leak probability P_{leaks} and number of spontaneous emission required for decelerating atoms $n(v) = v/v_{recoil}$, where v is a inital velocity of atoms. The efficiency is written as

$$p(v) = (1 - P_{leaks})^{n(v)} \simeq e^{-P_{leaks} \cdot n(v)} \tag{3.1}$$

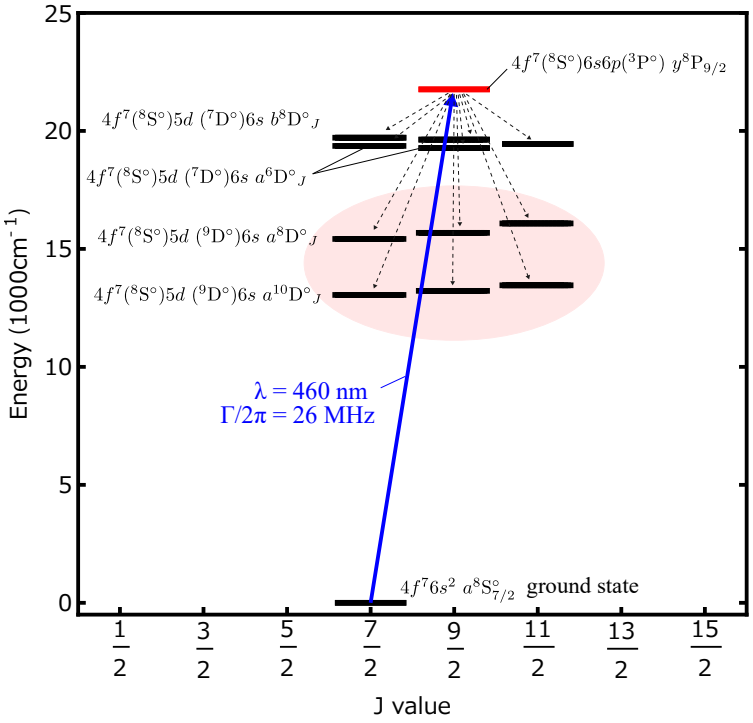

Figure 3.2: The 460-nm transition and possible decay channels from the $y^8P_{9/2}$ excited state to metastable states. Branching ratios to the lower six metastable states (shaded in light red) are measured in this work.

The velocity distribution of an atomic beam is characterized by a modified Maxwell-Boltzmann distribution [57]:

$$f_{AB}(v) = \frac{1}{2}\left(\frac{m}{2k_BT}\right)^2 v^3 \exp\left(-\frac{mv^2}{2k_BT}\right) \tag{3.2}$$

The total efficiency of Zeeman slowing is obtained by integration of the product of $p(v)$ and $f_{AB}(v)$ over v

$$\frac{\int_{v=0}^{v=v_0} p(v) f_{AB}(v)\ dv}{\int_{v=0}^{v=v_0} f_{AB}(v)\ dv} \tag{3.3}$$

where v_0 is a capture velocity of Zeeman slower.

Figure 3.3 shows the efficiency of Zeeman slowing as a function of optical leak probability calculated based on Eq. 3.3. Here, I set the temperature $T = 500\,°C$, where an effusive oven provide a sufficient atomic flux. v_0 is set to 360 m/s, which is the most probable speed at the temperature. The red marker indicates the optical leaks to the six metastable states measured in this work. As can be seen in Table 3.2 and Fig. 3.3, at least six repumping beams are required to increase the Zeeman slowing efficiency to an order of 0.1, where the optical leaks can be overcome by slightly increasing the oven temperature to provide sufficiently large flux. This result suggests a pessimistic outlook for Zeeman slowing using the 460-nm transition.

Transition ($y^8P_{9/2}-$)	Transition wavelength	Branching ratio
$a^{10}D_{7/2}$	1148 nm	$0.32(6) \times 10^{-4}$
$a^{10}D_{9/2}$	1171 nm	$1.08(6) \times 10^{-4}$
$a^{10}D_{11/2}$	1204 nm	$1.78(6) \times 10^{-4}$
$a^{8}D_{7/2}$	1577 nm	$0.24(5) \times 10^{-4}$
$a^{8}D_{9/2}$	1644 nm	$1.33(6) \times 10^{-4}$
$a^{8}D_{11/2}$	1760 nm	$5.72(10) \times 10^{-4}$
Total		$1.05(2) \times 10^{-3}$

Table 3.2: Estimated branching ratios [44].

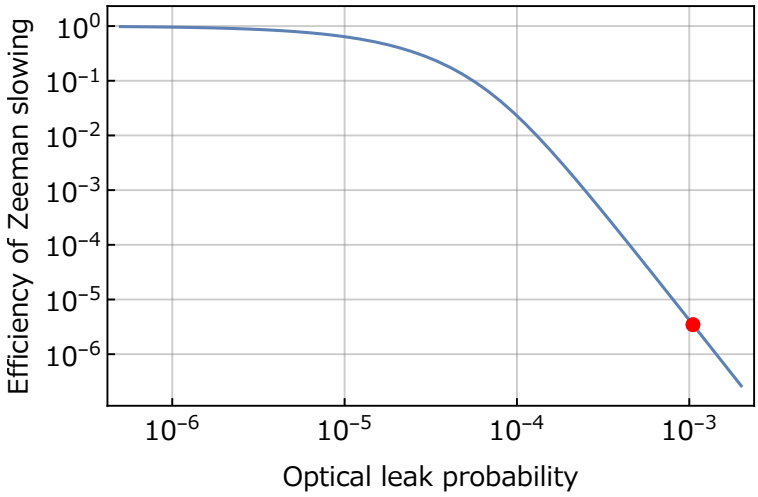

Figure 3.3: Efficiency of Zeeman slowing as a function of optical leak probability.The red marker indicates the optical leaks to the six metastable states measured in this work.

3.2 Laser cooling for metastable europium

3.2.1 Laser cooling scheme using a metastable state

Considering such large branching ratios, we conducted Zeeman slowing and MOT of europium using a cooling transition originated from a specific metastable state. Figure 3.4 shows energy levels of Eu including higher levels than those shown in Fig. 3.1. One can see that the transition $a^{10}D_{13/2}-z^{10}F_{15/2}$ is completely closed in electric-dipole approximation, where the wavelength and natural linewidth are 583 nm and 8.2 MHz, respectively [51]. This cyclic transition with MHz order of natural linewidth can be applicable to Zeeman slowing and MOT techniques. In order to prepare atoms in the $a^{10}D_{13/2}$ metastable state, we make use of the large branching ratios. The optical pumping path is shown in Fig. 3.4. By driving the 460 nm transition, atoms are pumped from the ground state into two intermediate states $a^{10}D_{9/2}$ and $a^{10}D_{11/2}$; then, they are pumped to $a^{10}D_{13/2}$ by driving the 507 nm and 513 nm transitions, respectively. The total transfer efficiency is estimated

as up to 19 % [1].

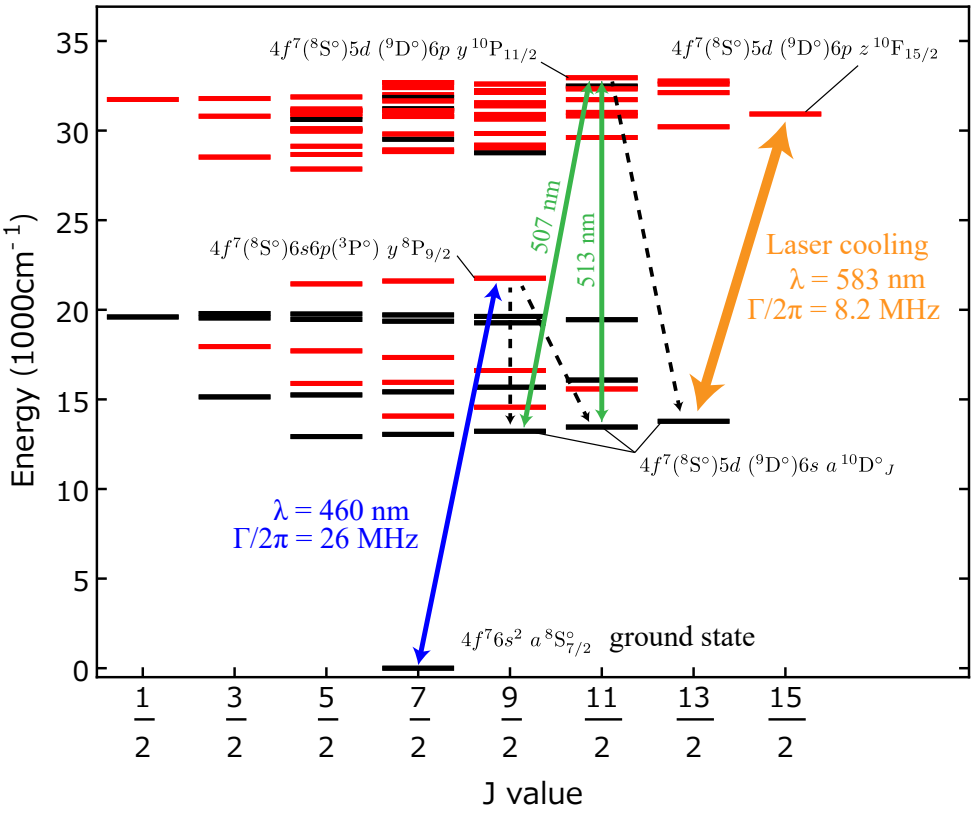

Figure 3.4: The energy levels of Eu [50, 51] showing the pumping and laser-cooling transitions. We have plotted the levels up to the energy of 32 948.41 cm^{-1}, which corresponds to the uppermost level $y^{10}P_{11/2}$ in this experiment. Red (black) horizontal lines indicate even (odd) parity states.

The Zeeman slowing and MOT for metastable europium using the 583-nm transition were first realized in our group and reported in Ref. [45]. Hereinafter, we call the MOT "yellow-MOT" to distinguish from the MOT for Eu atoms in the ground state described in Sec. 3.3. The experimental setup is schematically shown in Fig. 3.5. The atoms emitted from an effusive oven is first optically pumped to the $a^{10}D_{13/2}$ metastable stat by the three-color pumping light beams (at the wavelengths of 460, 507, and 513 nm) counter-propagating against the atomic beam. Then, the metastable atoms enter into Zeeman slower and decelerate by Zeeman slowing light at 583 nm. Slowed atoms in the $a^{10}D_{13/2}$ metastable state are then loaded to the MOT, which is formed in a quadrupole magnetic field provided by anti-Helmholtz coils and three pairs of counterpropagating, circularly polarized cooling-light beams at 583 nm. By using the setup mentioned above, up to 1×10^7 metastable ^{151}Eu atoms were trapped. Figure 3.6 shows a photograph of the yellow-MOT.

[1] Note that there is a more efficient optical pumping path using $a^8D_{11/2}$, where the branching ratio is the highest of the six. The total transfer efficiency is estimated as up to 51 % in Ref. [44]. However, this optical pumping requires a laser light at a wavelength of 599 nm, which cannot be produced directly from a laser diode. Therefore, we employed the optical pumping path using $a^{10}D_{9/2}$ and $a^{10}D_{11/2}$.

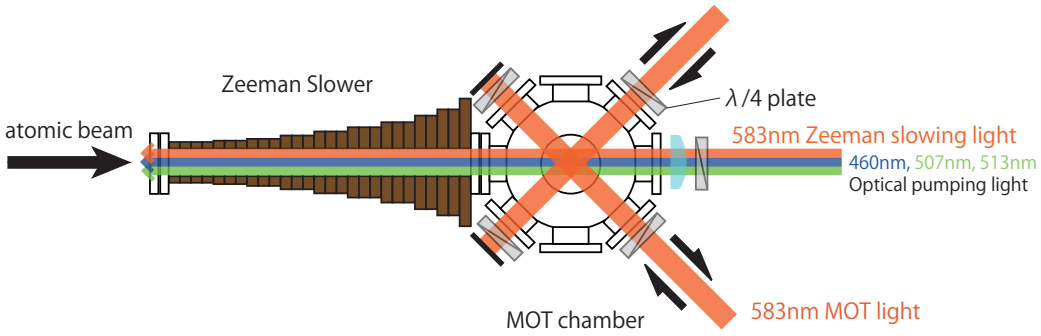

Figure 3.5: Setup for Zeeman slowing and yellow-MOT.

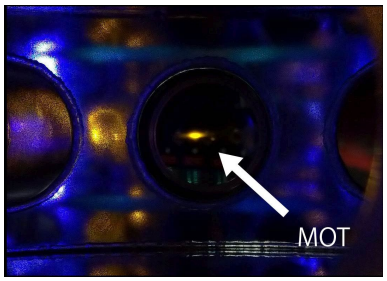

Figure 3.6: A photograph of the yellow-MOT

3.2.2 Towards Eu BEC

The europium atoms in the $|a^{10}\mathrm{D}_{13/2},\ F=9\rangle$ metastable state seem also a good candidate for dipolar BEC since it has a larger dipole moment of $11\,\mu_\mathrm{B}$ [58], which is larger than that of the most magnetic atoms of dysprosium, whose magnetic dipole moment is $10\,\mu_\mathrm{B}$. However, lifetime of atoms in the $|a^{10}\mathrm{D}_{13/2},\ F=9\rangle$ metastable state would be limited by two-body inelastic collision since the atoms are in the uppermost energy level in the hyperfine manifold. In addition, the atoms in $a^{10}\mathrm{D}_{13/2}$ decay to the lower states of the fine structure $a^{10}\mathrm{D}_{11/2}$ and $a^{10}\mathrm{D}_{9/2}$ with a time constant of $\sim 400\,\mathrm{ms}$ via blackbody radiation. It was first suggested in this MOT experiment [45] and confirmed by measuring a lifetime of europium atoms in $a^{10}\mathrm{D}_{13/2}$ in a magnetic trap [59]. Losses induced by blackbody radiation are inevitable in a room-temperature chamber; therefore, europium atoms in the $a^{10}\mathrm{D}_{13/2}$ metastable state are not suitable for producing a BEC. In order to conduct dipolar BEC experiments using europium atoms, we have to pump back the metastable Eu atoms to the ground state and produce a europium BEC in the ground state.

3.3 Strategy for laser cooling of europium in the ground state

3.3.1 Introduction

In order to create a Eu BEC in the ground state, one should prepare cold ground state Eu atoms in an optical dipole trap (ODT) [2]. Through successive evaporative cooling, a BEC would be obtained. Although cold Eu atoms in the $a^{10}D_{13/2}$ metastable states were previously obtained, preparing ground state Eu atoms in ODT is still challenging since there is no reliable method.

In this study, I planed to employ MOT for Eu atoms in the ground state by using a narrow-line cooling transition with a natural linewidth of 97 kHz and a wavelength of 687 nm. Since its Doppler limit is as low as 2.3 μK, the MOT would provide us with good starting conditions for direct loading to an ODT. Hereinafter, we call this narrow-line MOT "red-MOT" to distinguish from the "yellow-MOT", which is described in Sec. 3.2. We employ simultaneous MOT for the metastable and ground-state atoms. The trapped metastable atoms are successively pumped back to the ground state and then continuously loaded to the red-MOT. The details of this procedure is explained in next subsection.

The biggest concern in the red-MOT is optical leaks from $z^{10}P_{9/2}$ excited states to the three metastable states (see Fig. 3.1), where the branching ratios are unknown so far. If the optical leak probability is too high, they shorten a lifetime of the red-MOT, which limits a number of trapped atoms or loading efficiency from the red-MOT to an ODT. To plug the optical leaks, we planed to repump atoms in the three metastable states to the ground state, which is described in Sec. 3.3.3.

3.3.2 Red-MOT procedure

Figure 3.7 shows the schematic of our laser cooling procedure. I explain from producing the yellow-MOT. We start from a hot atomic beam of Eu in the ground state. Atoms in the ground state $a^8S^\circ_{7/2}$ are transferred to the metastable state $a^{10}D^\circ_{13/2}$ as described below. By driving the 460 nm transition, atoms are pumped from the ground state into two intermediate states $a^{10}D^\circ_{9/2}$ and $a^{10}D^\circ_{11/2}$; then, they are pumped to $a^{10}D^\circ_{13/2}$ by driving the 507 nm and 513 nm transitions, respectively. The atoms in $a^{10}D^\circ_{13/2}$ are then Zeeman slowed and captured in a yellow-MOT using the 583-nm transition. The captured metastable atoms are successively pumped back to the ground state by driving two transitions at the wavelengths of 609 nm and 1204 nm. The pumping-back efficiency is estimated as 94 % [44, 51]. Pumped back atoms are cooled and trapped in the red-MOT using the 687-nm cooling transition. Note that this series of optical pumping and laser cooling processes are executed simultaneously. Atoms in the ground state are thus loaded to the red-MOT continuously.

[2] A magnetic trap is also used commonly to create an alkali metal BEC. However, in the case of Eu, magnetic trap is not suitable since inelastic dipolar relaxation loss would be much larger than those of alkali metals due to its large dipole moment and large atomic mass. It makes evaporative cooling inefficient and disturbs increasing phase-space density of atoms.

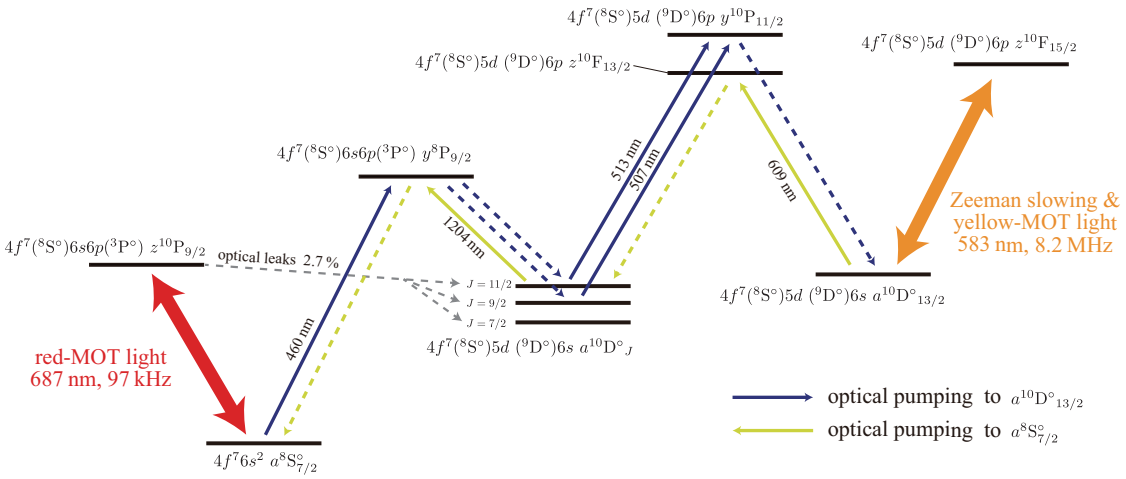

Figure 3.7: Energy levels and transitions of Eu relevant for our laser cooling procedure [51, 52]. Solid lines indicate laser-driven transitions and dashed lines indicate spontaneous decay channels.

3.3.3 Repumping scheme

The cooling transition at 678 nm has optical leaks from the excited state $z^{10}P_{9/2}$ to three metastable states $a^{10}D^\circ_{7/2}$, $a^{10}D^\circ_{9/2}$, and $a^{10}D^\circ_{11/2}$ whose transition wavelengths are 6.6, 7.5, and 9.0 μm, respectively [3]. Here, I chose $y^8P_{9/2}$ state as a intermediate state of our repumping, since the branching ratios from the $y^8P_{9/2}$ is well studied in our previous work (see Table 3.2) and high repumping efficiency would be obtained with three-color laser lights with wavelenghts of 1148, 1171, and 1204 nm.

Figure 3.8 shows energy levels and transitions of ^{151}Eu relavant for our repumping scheme including hyperfine structure. The laser cooling transition is $|a^8S_{7/2}, F = 6\rangle \leftrightarrow |z^{10}P_{9/2}, F = 7\rangle$. Considering selection rules that only $\Delta F = 0, \pm 1$ transitions are allowed, excited atoms in $|z^{10}P_{9/2}, F = 7\rangle$ leaks to six hyperfine state $|a^{10}D_{7/2}, F = 6\rangle$, $|a^{10}D_{9/2}, F = 6, 7\rangle$, and $|a^{10}D_{11/2}, F = 6, 7, 8\rangle$. Here we omit the repumping from the state $|a^{10}D_{11/2}, F = 6\rangle$, since the transition probability of $|z^{10}F_{9/2}, F = 7\rangle \rightarrow |a^{10}D_{11/2}, F = 6\rangle$ is only 0.15 %[4] of that of $|z^{10}F_{9/2}, F = 7\rangle \rightarrow |a^{10}D_{11/2}, F = 8\rangle$, which is comparable with the optical leak probability from $y^8P_{9/2}$ to other metastable states referred to as "others" in Fig. 3.8. This means that the repumping of atoms in $|a^{10}D_{11/2}, F = 6\rangle$ has small influence on the lifetime of the red-MOT. One can estimate this overall repumping efficiency of the scheme as up to ~ 99.9 %.

Atoms should be repumped to the ground state before they diffuse outside of the red-MOT capture range. To estimate sufficient power of the repumping light, I also calculated optical pumping rate under any repumping light intensity by solving λ-type optical Bloch equations. In case Rabi frequency Ω for the repumping transition is much smaller than

[3] The decay rates to the three metastable states were not known when I planed this cooling scheme, and measured in this work by using the red-MOT (see Sec. 5.5). The sum of the decay rates was estimated as $1.64(5) \times 10^4\,s^{-1}$, which corresponds to a branching fraction of 2.7 %.

[4] This ratio is calculated by using Clebsch–Gordan coefficients [60].

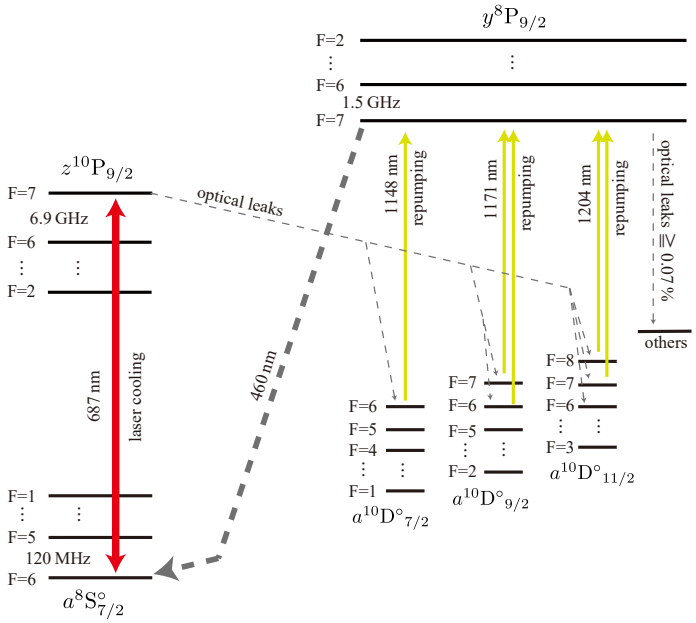

Figure 3.8: Energy levels and transitions of ^{151}Eu relevant for our repumping scheme including hyperfine structures. Solid lines indicate laser-driven transitions and dashed lines indicate spontaneous decay channels. Hyperfine splittings are calculated based on hyperfine constants in Refs. [38, 61]

decay rate of the excited state Γ, the repumping rate is written as

$$R_{repump} \simeq \Omega^2/\Gamma = \alpha \times I_0 \tag{3.4}$$

where α is a coefficient and I_0 is a intensity of the incident light. The α for each repumping transition is calculated and summarized in Table 3.3. Here we assume random polarization of the repumping light. The required power for the reupmping is a few mW, if one assumes the lowest α of the five, 3 mm diameter of repumping beam, and repumping 99 % of atoms within 1 ms.

transition	λ (nm)	A_{ik} (s^{-1})	$F \to F'$	α ($s^{-1}/(mW/cm^2)$)
$a^{10}D_{7/2} \to y^8P_{9/2}$	1148	$0.5(1) \times 10^4$	$6 \to 7$	0.45×10^3
$a^{10}D_{9/2} \to y^8P_{9/2}$	1171	$1.7(1) \times 10^4$	$7 \to 7$	1.30×10^3
			$6 \to 7$	0.10×10^3
$a^{10}D_{11/2} \to y^8P_{9/2}$	1204	$2.9(2) \times 10^4$	$8 \to 7$	2.07×10^3
			$7 \to 7$	0.13×10^3

Table 3.3: Repumping transition parameters for the red-MOT. A_{ik} is a transition probability for the transition. α is the coefficient in Eq. 3.4.

Chapter 4: Experimental setup

This chapter describes experimental setup used to produce Eu BEC.

4.1 Vaccum chamber design

Figure 4.1 gives an overview of the vacuum system. The Eu atoms are produce from an effusive oven. They are decelerated through the Zeeman slower and trapped in the main chamber, where further cooling to BEC is performed. Each individual part of the vacuum system is explained in the following sections.

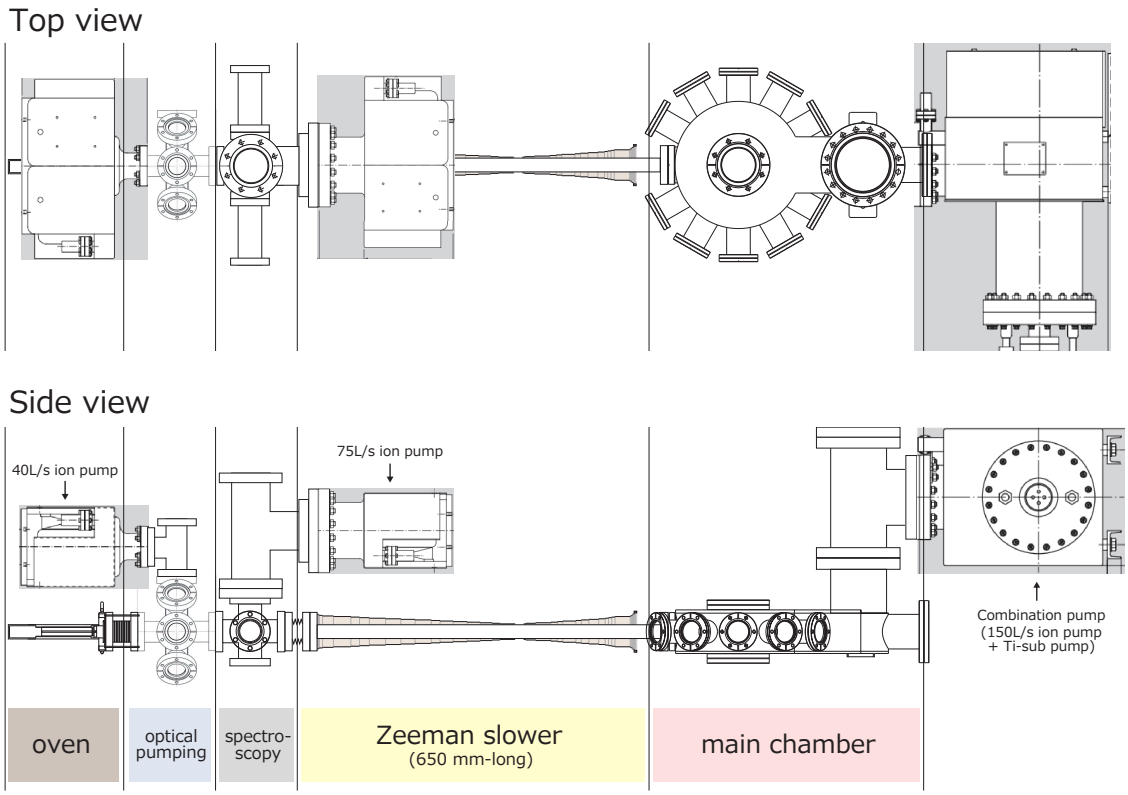

Figure 4.1: Drawing of the vacuum system. Note that some parts (ion gauges, valves, an atomic beam shutter, and some vacuum components) are not drawn to make it easy to see.

4.1.1 Atomic oven

We use an atomic oven for providing sufficient flux of an atomic beam since saturated vapor pressure of Eu is considerably low at room temperature (see Fig. 2.2). The design of the oven is shown in Fig. 4.2 and its picture is shown in Fig. 4.3. Eu metal chunks (weight 5 g, purity 99.9 %) are enclosed in the oven. They are heated up to the required temperature by heating nichrome wires wound around the $\phi 26$ cylinder, which is covered by a heat insulator made of ceramic fiber. The annealed cooper tube is attached to the ICF flange for water cooling so that temperature of a port aligner connected to this oven on the ICF flange will not exceed an absolute maximum rating temperature of 200 °C.

The atomic beam is collimated by a nozzle with a length of 100 mm and diameter of 2.5 mm. We operate the oven at a temperature of 500 °C, where an atom flux is estimated as 3×10^{11} atoms/s[1] at the spectroscopy section by using equations in Ref. [57]. The flux is confirmed experimentally by using an absorption spectroscopy with the 460-nm transition, whose results is consistent with the estimation.

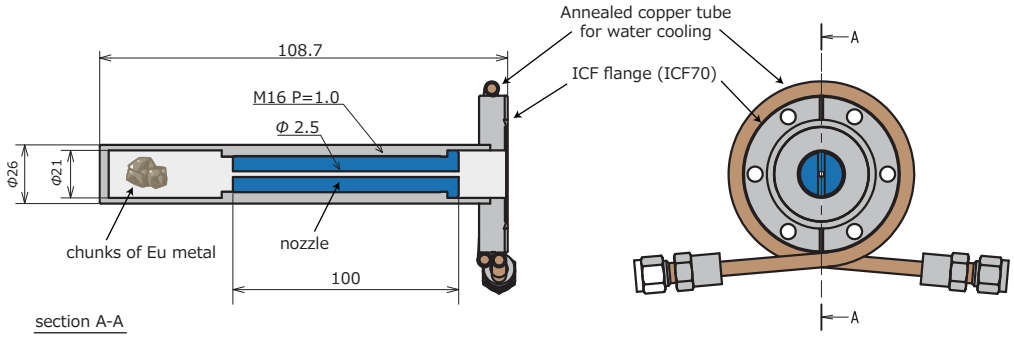

Figure 4.2: Drawing of the Eu effusive oven. Left one is a section view, whereas right one is a front view. Heating wires and a heat insulator are not shown here.

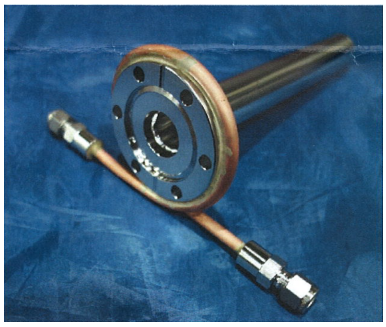

Figure 4.3: A picture of the Eu oven

4.1.2 Optical pumping section

This section is for optical pumping of atoms in the ground sate to $a^{10}D_{9/2}$ and $a^{10}D_{11/2}$ metastable states. The optical pumping is performed by irradiating 460-nm laser light to the atomic beam perpendicularly through ICF70 AR coated viewports.

An atomic beam shutter is installed in this section. The shutter stops an atomic beam to avoid inelastic collisions of atoms in trap with an atomic beam, or to prevent the viewport for Zeeman slowing from being coated with the Eu atomic beam when an experiment is not running. Figure 4.4 shows pictures of an atomic beam shutter. The atomic beam is switched on and off by rotating the U-shaped shutter connected to a magnetic coupling rotary feedthrough[2]. The rotation of the shutter is performed by a stepping motor. The switching time is within 150 ms.

[1] Note that in the red-MOT experiment in chapter 4, we can use only ^{151}Eu isotope in the ground state $F = 6$ hypefine manifold, whose flux is about 13 % of the total flux. Note that about half of atoms in the spectroscopy section cannot reach to the main chamber since they spreed and collide with Zeeman tube. A resulting flux available in this experiment is about 1×10^{10} atoms/s.

[2] model 954-7605, from Canon Anelva Corp.

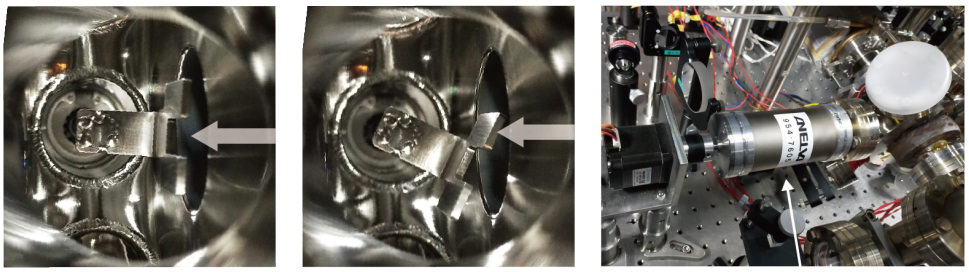

(a) shutter on (b) shutter off (c) rotary feedthrough

Figure 4.4: (a) and (b) shows an atomic beam shutter installed in the vacuum chamber, whose position is on and off, respectively. The arrow indicates an atomic beam. (c) A picture of a rotary feedthrough installed in the optical pumping section.

4.1.3 Spectroscopy section

Spectroscopy section is required for finding out the resonances of Eu for various transitions since our experiment use many optical transitions and some of them are difficult to identify the resonances without a high flux atomic beam spectroscopy. Once the resonances are identified, the laser frequencies can be stabilized to the resonances by using reference cavities. Thus, we do not use this section in daily experiments.

4.1.4 Zeeman slower

The ZS is designed for decelerating Eu atoms in $a^{10}\mathrm{D}_{13/2}$ metastable state by using the 583-nm transition. The ZS vacuum tube has a total length of 651 nm and a inner diameter of 22 mm. We adopted spin-flip type ZS, which enables us to decelerate Eu atoms with lower absolute values of the magnetic field than increasing type ZS. The ZS can decelerate atoms with a speed below 240 m/s, which corresponds to the lower 15 % of the velocity distribution. See Ogata's master thesis [62] (written in Japanese) for more details on this ZS.

4.1.5 Main chamber

Yellow-MOT, red-MOT, and evaporative cooling to BEC is performed in the main chamber. To obtain BEC via evaporative cooling, the collisional loss rate between trapped atoms and the background gas should be typically smaller than $0.1\,\mathrm{s}^{-1}$, which means the pressure of the main chamber should be lower than 10^{-10} Torr as a rule of thumb [63,64]. To reach ultra-high vacuum regime, we baked out the whole vacuum system at a temperature of 200 °C for 10 days. To prevent an atomic oven operating at 500 °C from increasing a pressure of the main chamber, differential pumping tubes are inserted between optical pumping section and spectroscopy section, and between spectroscopy section and Zeeman slower section, which maintain a pressure difference between optical pumping section and main chamber section of up to three order of magnitude. The resultant pressure of the main chamber with operating an atomic oven is lower than 5×10^{-12} Torr, which is measured

by an ion gauge[3]. The lifetime of trapped atoms in a ODT is experimentally measured to be longer than 150 s. It is sufficiently long lifetime for producing a BEC.

4.2 Laser systems

For the production of a Eu BEC, we use 10 colors of laser lights, which are listed in Table 4.1. Each laser system is described in the following sections.

Wavelength	Purpose	Transition	laser type
460 nm	optical pumping abs. imaging	$a^8S_{7/2} \rightarrow y^8P_{9/2}$	SHG ECDL
507 nm	optical pumping	$a^{10}D_{9/2} \rightarrow z^{10}F_{11/2}$	SHG
513 nm	optical pumping	$a^{10}D_{11/2} \rightarrow z^{10}F_{11/2}$	ECDL
583 nm	ZS yellow-MOT	$a^{10}D_{13/2} \rightarrow z^{10}F_{15/2}$	Dye laser
609 nm	optical pumping	$a^{10}D_{13/2} \rightarrow z^{10}P_{13/2}$	SHG
687 nm	red-MOT	$a^8S_{7/2} \rightarrow z^{10}P_{9/2}$	ECDL
1148 nm	repumping	$a^{10}D_{7/2} \rightarrow y^8P_{9/2}$	ECDL
1171 nm	repumping	$a^{10}D_{9/2} \rightarrow y^8P_{9/2}$	DFB laser
1204 nm	repumping	$a^{10}D_{11/2} \rightarrow y^8P_{9/2}$	ECDL
1550 nm	ODT	-	fiber laser & amp

Table 4.1: List of lasers used in the experiment.

[3] UHV-24p, Agilent technologies

4.2.1 460 nm

We use two 460-nm laser lights. The one laser light is generated by a second harmonic generation (SHG) system shown in Fig. 4.5, which is used for optical pumping (see Fig. 3.7) and absorption imaging. The fundamental light source is a homemade external cavity diode laser (ECDL) at 919 nm using Thorlabs' LD chip[4]. It is then amplified by a tapper amplifier[5] (TA). Between the ECDL and TA, an acoustic optical modulator (AOM) is inserted to protect the ECDL from feedback by the mode-matched beam of the TA. Its frequency is doubled in a bow-tie ring cavity with a PPKTP crystal, whose output power is typically $\sim 150\,\mathrm{mW}$. Most of the laser power is used for the optical pumping and the rest is used for absorption imaging. The laser frequency is stabilized by PDH locking to a transfer cavity so that the absorption imaging light resonant to the $F = 6 \to F' = 7$ transition.

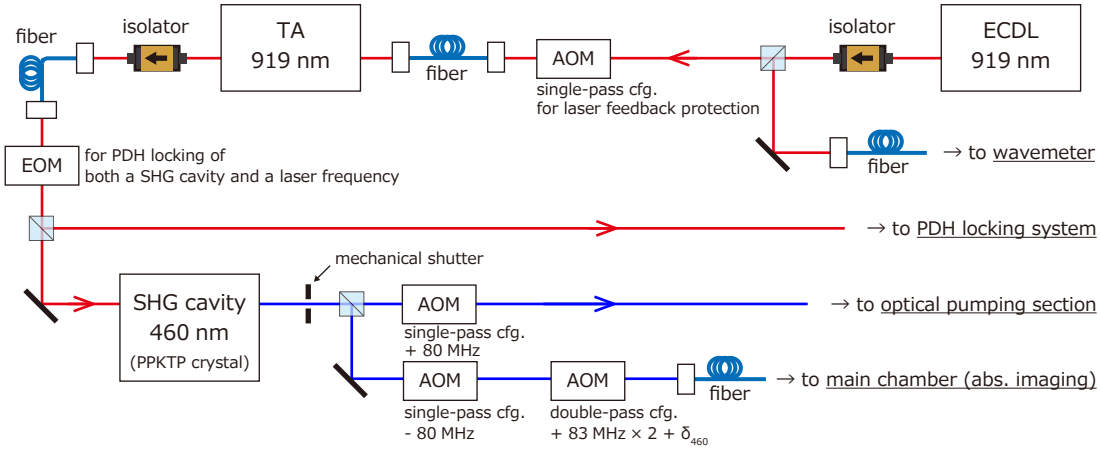

Figure 4.5: The 460-nm laser setup (SHG)

The other 460-nm laser light is directly generated by a homemade ECDL using Nichia's LD chip[6]. It is used for spin polarization with two-color pumping light tuned to $F = 5 \to F' = 6$ and $F = 6 \to F' = 6$, respectively. The setup for the 460-nm ECDL is shown in Fig. 4.6. The two-color light which has a frequency difference of 120.7 MHz is produced by the second AOM, where a 0-order beam and a $+1st$-order beam are overlapped. The power ratio of the two beams is set as $P_{F=5\to F'=6} : P_{F=5\to F'=6} = 4 : 6$ for optimal spin polarization. The laser frequency is stabilized PDH locking to a ULE cavity.

[4] M9-915-0200, Thorlabs Inc.
[5] TA-0920-2000, m2k-laser GmbH
[6] NDB4216E, Nichia Corp.

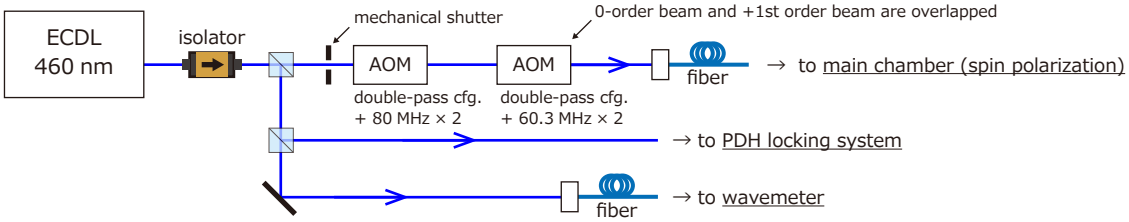

Figure 4.6: The 460-nm laser setup (ECDL)

4.2.2 507 nm and 513 nm

The 507-nm light is generated by a SHG system, which we borrowed from Yb group in our laboratory (It will be replaced by ECDL system in future.). The 513-nm light source is a ECDL using Nichia's LD chip[7]. Both lights are used for optical pumping (see Fig. 3.7). They are combined though PBS and propagate to main chamber. Note that their frequencies are not stabilized since their optical pumping efficiencies are not changed over a few hundred MHz drift.

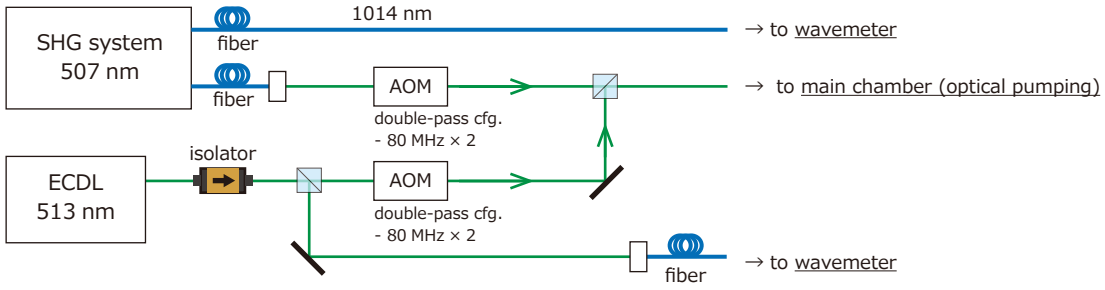

Figure 4.7: The 507 nm and 513 nm laser setup.

4.2.3 583 nm

The 583-nm light source is a continuous-wave ring-cavity dye laser[8] using rhodamine 6G as lasing medium. The dye laser is pumped by a 10 W solid-state laser[9] at 532 nm. The pumping power is usually regulated around 4 W, which provides longer lifetime of the dye and sufficiently high output power (>400 mW) at 583 nm.

The 583-nm dye laser is used for laser cooling of Eu in the $a^{10}D_{13/2}$ metastable state. The setup is shown in Fig. 4.8. The output beam from the dye laser is first picked up a several mW power for wavemeter and PDH locking system. Then, the beam passes through a mechanical shutter and split into two; one is for absorption imaging, ZS, and yellow-MOT (① cooling) and the other one is for hyperfine repumping (② HF repumping). The fiber coupled electro-optic phase modulator[10] (EOM) generates a sideband for the hyperfine repumping. On-resonant HF repumping light tuned to $F = 8 \rightarrow F' = 9$ overlaps with the MOT beams detuned by δ_{583} from the $F = 9 \rightarrow F' = 10$ cyclic transition.

[7] NDG4216, Nichia Corp.
[8] 899 dye ring laser, Coherent Inc.
[9] Verdi V10, Coherent In.
[10] WPM-K0583-P48P48-AL0, AdvR Inc.

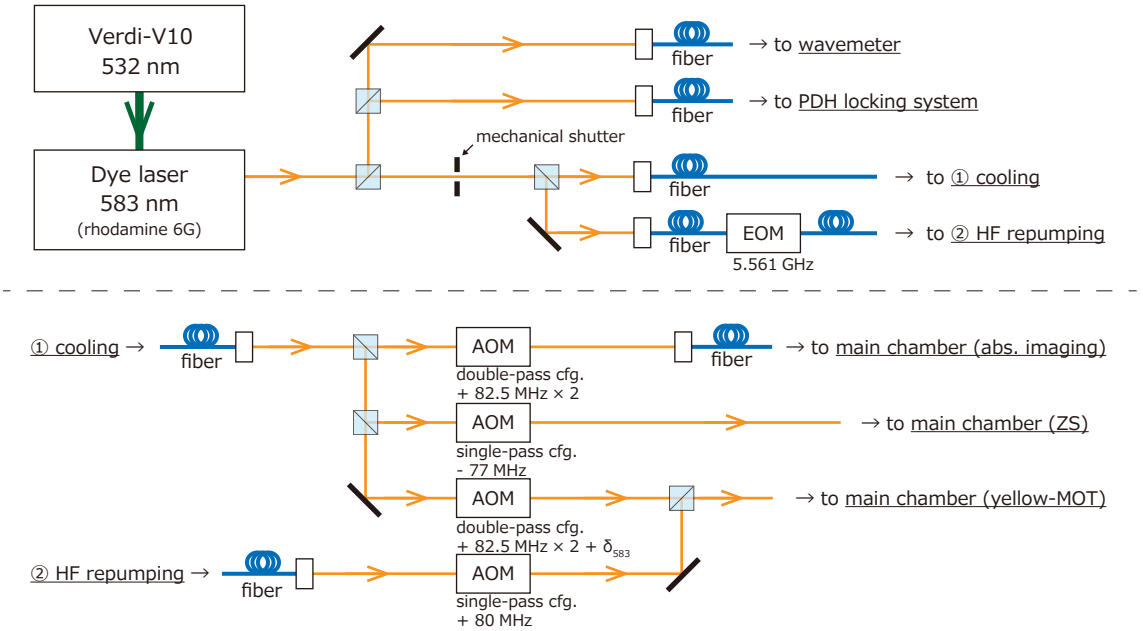

Figure 4.8: The 583 nm laser setup.

4.2.4 609 nm

The 609-nm laser light is generated by SHG system shown in Fig. 4.9. The fundamental light source is a homemade ECDL at 1217 nm made of Thorlabs' gain chip[11], which has a built-in optical isolator and PM fiber output. The frequency of the fundamental ligth is doubled though a custom-made PPLN waveguide[12]. The output power of the waveguide is 180 μW with the fundamental laser power of 25 mW. The frequency of the laser is stabilized by PDH locking to a transfer cavity. The switching of the 609-nm beam is achieved by an AOM. The output power is regulated (4 μW at red-MOT)

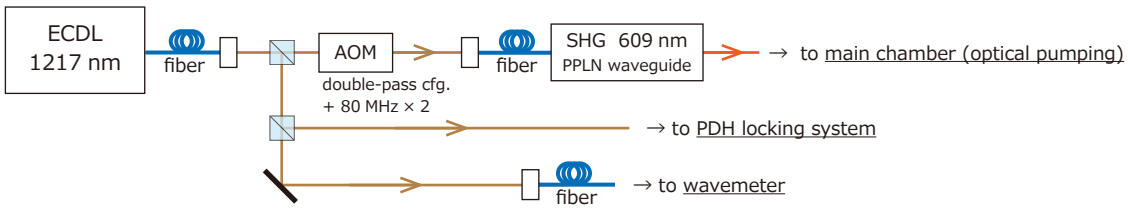

Figure 4.9: The 609 nm laser setup.

[11] SAF1175S, Thorlabs Inc.
[12] Waveguide Mixer, HC photonics Corp.

4.2.5 687 nm

The 687-nm laser light source is a homemade ECDL using a Thorlabs' LD chip[13]. It is amplified by a tapered-amplifier[14] and propagates to main chamber though an optical fiber as shown in Fig. 4.10. A maximum fiber output power of 80 mW can be used for red-MOT. The frequency and power of the MOT beam are controlled by an AOM.

For red-MOT operation, the laser linewidth and frequency drift during experiment have to be lower than 97 kHz, which is given by the natural linewidth of the 687-nm transition. The demand is satisfied by PDH technique using a ULE cavity, whose cavity-linewidth is 150 kHz at the wavelength of 687 nm. The stabilized linewidth is below 33(8) kHz. The long-term frequency drift is measured to be 7.9 kHz/day by cold Eu atom spectroscopy over a time scale of 250 days. The drift is compensated by changing the frequency driving the AOM feedforwardly.

The stabilized 687-nm laser light is also used for stabilizing transfer-cavity lengths (see Sec. 4.2.8) and for probe light to measure a differential light shift induced in a ODT (see Sec. 6.4).

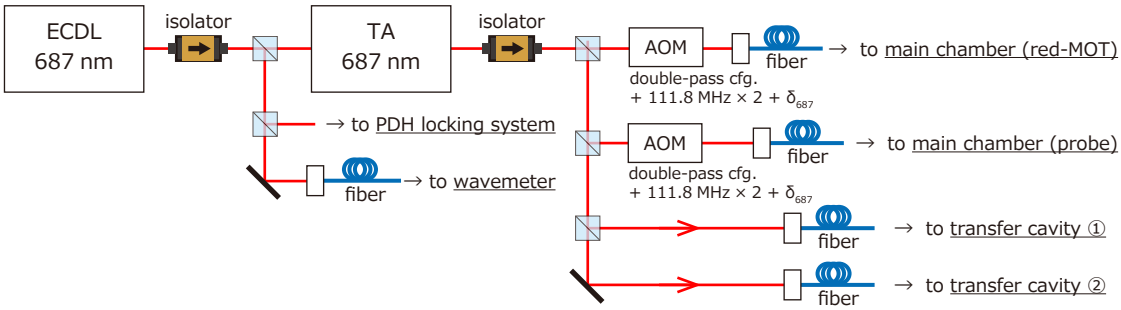

Figure 4.10: The 687 nm laser setup.

4.2.6 1148 nm, 1171 nm, and 1204 nm

Three color IR repumping laser sources of 1148 nm, 1171 nm, and 1204 nm are a custom-made ECDL[15], two DFB lasers[16], and two homemade ECDLs[17], respectively. The two of each 1171 nm and 1204 nm laser source are used to pump two hyperfine transitions, respectively (see Fig. 3.7). All IR lasers has built-in optical isolator, and PM or SM fiber output.

The laser setup is shown in Fig. 4.11. The laser frequencies are stabilized by PDH locking to transfer cavities. The switching of the repumping beams are achieved by AOMs.

[13] HL6750MG, Thorlabs Inc.
[14] EYP-TPA-0690-00500-2003-CMT02-0000, eagleyard Photonics GmbH
[15] DL pro, Toptica photonics Inc.
[16] DFB-1171-PM-30-OI, Innolume GmbH
[17] SAF1175S, Thorlabs Inc.

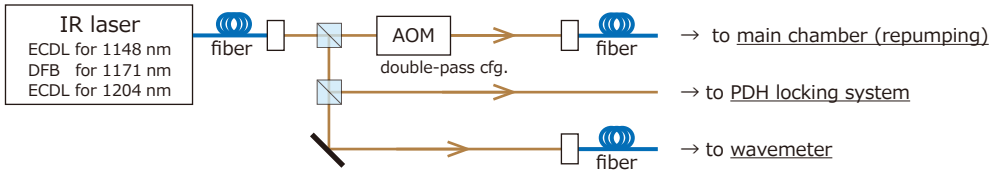

Figure 4.11: The IR lasers setup.

4.2.7 1550 nm

We use a 1550 nm laser for ODT. The laser light source is a single frequency DFB fiber laser[18], which is amplified by a erbium-doped fiber amplifier[19] with a maximum output power of 15 W. The setup is shown in Fig 4.12. The first order diffracted beam from the first AOM is used for a horizontal ODT, whereas the zero order diffracted beam is recycled to a vertical ODT. To avoid undesired heating of atoms due to interference between horizontal and vertical ODT, the frequency detuned 160 MHz from each other. Both laser beam powers are controlled and stabilized by the AOMs.

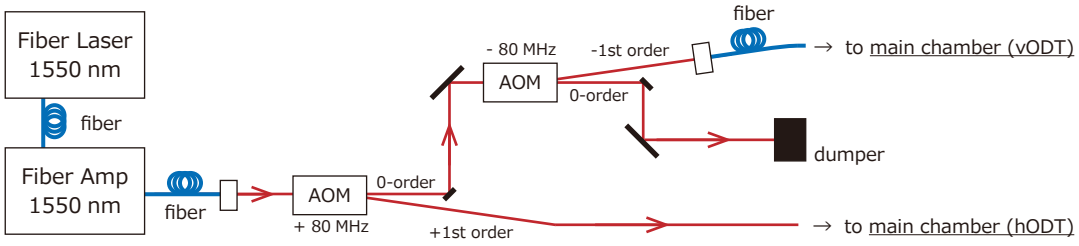

Figure 4.12: The 1550 nm laser setup.

4.2.8 Reference cavities & PDH locking system

In this experiment, we have to stabilize 10 laser frequencies. The demand is satisfied by using the Pound–Drever–Hall (PDH) technique [65] with three reference cavities: one ultra-low expansion (ULE) cavity and two transfer cavities.

ULE cavity

One reference cavity is a custom-made ULE cavity [20], whose spacer is made of ULE glass. The specification of the cavity is listed in Table 4.2. To achieve sufficiently high stability the ULE cavity is stored in vacuum and shielded from outside temperature fluctuations by double aluminum shields (see Fig. 4.13). This cavity is a frequency standard of our experiment. Frequencies of 687 nm, 583 nm, and 460 nm laser are stabilized to the ULE cavity.

[18] Koheras Adjustik E15 Power, NKT Photonics A/S
[19] CEFA-C-BO-HP-PM-42-NL1-OM1-B301-FA-C1, Keopsys Inc.
[20] manufactured by FiveNine Optics Inc., the spacer is made of corning 7973ULE zero crossing 25 ∼ 40 °C

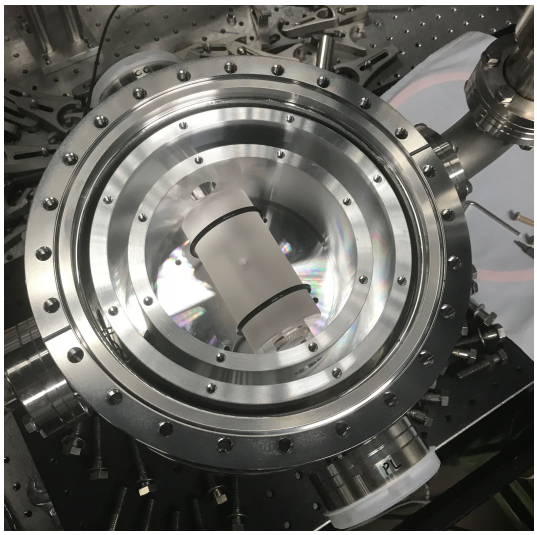

Figure 4.13: A photo of ULE cavity in vacuum chamber.

L	FSR
10 cm	1.5 GHz

λ	R	Finesse	δ_ν
460 nm	99.62%	800	1.8 MHz
507 nm	99.65%	900	1.7 MHz
513 nm	99.64%	900	1.7 MHz
583 nm	99.65%	900	1.7 MHz
687 nm	99.969%	10000	150 kHz

Table 4.2: specification of the ULE cavity.

transfer cavity

The other two reference cavities are transfer cavities. The cavity lengths are stabilized by frequency stabilized 687 nm laser. The reference cavities are used to stabilize frequency of 919 nm, 1217 nm, 1148 nm, 1171 nm, and 1204 nm laser lights.

Chapter 5: Narrow-line magneto-optical trapping for europium

5.1 Setup for red-MOT

Figure 5.1 shows setup for red-MOT. Europium atoms emitted from an effusive oven are first optically pumped to $a^{10}\mathrm{D}_{9/2}$ and $a^{10}\mathrm{D}_{11/2}$ metastable states by driving 460 nm transition in the optical pumping section. The beam has a power of ~ 100 mW and retro-reflected. To maximize optical pumping efficiency, we shape the laser beam into an ellipse with a diameter of 7 mm $\times$ 30 mm to maximize the interaction region, where the major axis is aligned to the atomic beam direction. In addition, we apply a bias magnetic field of $\sim$1 G along the pumping beam and make the pumping beam polarization σ_+. In this condition, we can pump atoms with a specific $|F = 6, m_F = 6\rangle \rightarrow |F' = 7, m_F = 7\rangle$ cyclic transition, where the Clebsch–Gordan coefficient is 1. This enables us to drive the 460 nm transition with 2.6 times higher frequency than random polarization condition. The frequency of the pumping laser is slightly red-detuned ($\sim$ 6 MHz) to avoid undesired heating.

Atoms in $a^{10}\mathrm{D}_{9/2}$ and $a^{10}\mathrm{D}_{11/2}$ metastable states are optically pumped to $a^{10}\mathrm{D}_{13/2}$ metastable state by 507 nm and 513 nm, respectively. Then they are decelerated through the Zeeman slower and trapped in a yellow-MOT. The beam diameter was about 25mm and truncated by a circular aperture of 21.6 mm diameter.

Trapped $a^{10}\mathrm{D}_{13/2}$ metastable atoms are pumped back to the ground state continuously by 609 nm and 1204 nm laser light. The beam diameter of the pumping light at 609 nm matched the size of the yellow-MOT of about 500 μm so that cooled atoms were selectively pumped back.

The narrow-line red-MOT was formed in the same magnetic field as the yellow-MOT. The cooling laser beams overlapped the 583-nm beams with the same polarization and beam diameter. The intensity ratio of the laser beams propagating in axial and radial directions of the coil was set as 2:1. We have added 1148 nm, 1171 nm, 1204 nm lasers for repumping. Each repumping light beam was introduced to the MOT chamber and was retroreflected, where the beam diameter and the power were set as 3mm and $\sim$1 0mW, respectively.

The number of trapped atoms was determined by an absorption imaging technique using the 460 nm transition with spin polarization. We turned off all the lights and quadrupole magnetic field after loading the atoms and applied a magnetic field of approximately 10^{-4} T along the probe axis. Then, atoms were optically pumped to the $|F = 6, m_F = 6\rangle$ Zeeman sublevel by a two-color σ_+ polarized light pulse tuned to $F = 5 \leftrightarrow F' = 6$ and $F = 6 \leftrightarrow F' = 6$ transitions. Subsequently, the polarized atoms were illuminated by a σ^+ polarized probe laser beam near-resonant on $|F = 6, m_F = 6\rangle \leftrightarrow |F' = 7, m_{F'} = 7\rangle$ transition. The absorption by the atoms casts a shadow on an imaging device. We confirmed that the degree of the spin polarization is sufficient for determining the number of atoms within a few percent errors by comparing the optical depth of two images obtained by σ_+ and σ_- polarized probe beams.

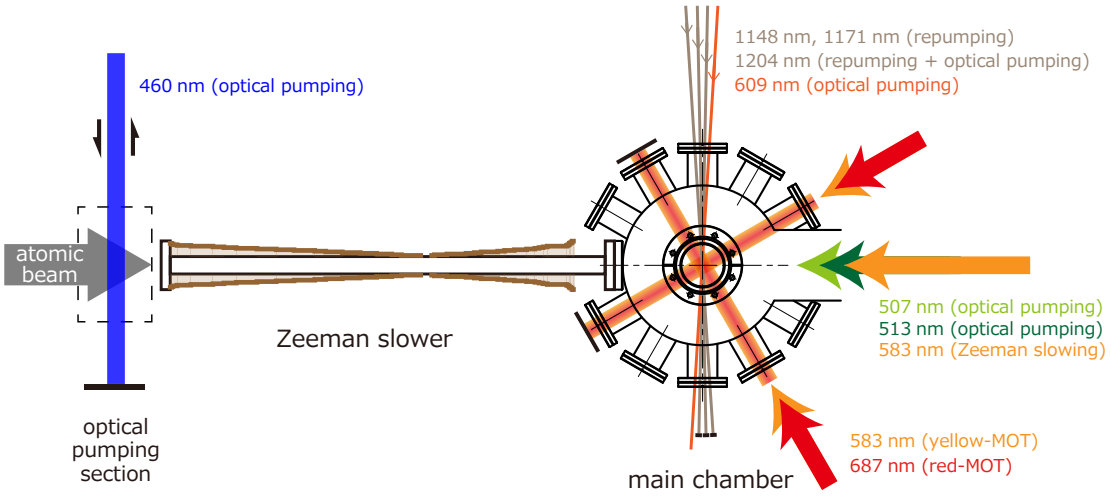

Figure 5.1: Setup for Red-MOT

5.2 Number of trapped atoms

The number of atoms in our red-MOT was maximized under the following experimental conditions. The axial magnetic field gradient was set to $\partial B_z/\partial z = 3 \times 10^{-2}\,\mathrm{T/m}$. The detuning and total intensity of the cooling laser for the yellow-MOT were $-1.75\,\Gamma_{583}$ and $3.7\,I_{s,583}$, respectively, whereas these values for the narrow-line red-MOT were $\delta_{687} = -13\,\Gamma_{687}$ and $I_{687} = 40\,I_{s,687}$. Here, $I_{s,583} = 5.4\,\mathrm{mW/cm^2}$, and $I_{s,687} = 3.9\,\mu\mathrm{W/cm^2}$ were the saturation intensities for the cooling transitions. The intensity of the optical pumping light at 609 nm was set to $1\,\mathrm{mW/cm^2}$, where the optical pumping rate is estimated as $10^5\,\mathrm{s^{-1}}$.

Figure 5.2 (a) summarizes the number of trapped atoms after 4 s of loading as a function of the detuning δ_{687} and the intensity I_{687}. The maximum number of atoms is obtained around $\delta_{687} = -13\,\Gamma_{687}$ and $I_{687} = 40\,I_{s,687}$. The loading and decay curves of the red-MOT under the optimal conditions are shown in Fig. 5.2 (b) and (c), respectively. From curve fitting [cite], we obtained a loading rate $R = 6 \times 10^7$ atoms/s, a one-body loss rate of $1/\tau = 0.38\,\mathrm{s^{-1}}$, and a two-body loss rate of $\beta = 7 \times 10^{-11}\,\mathrm{cm^3/s}$.

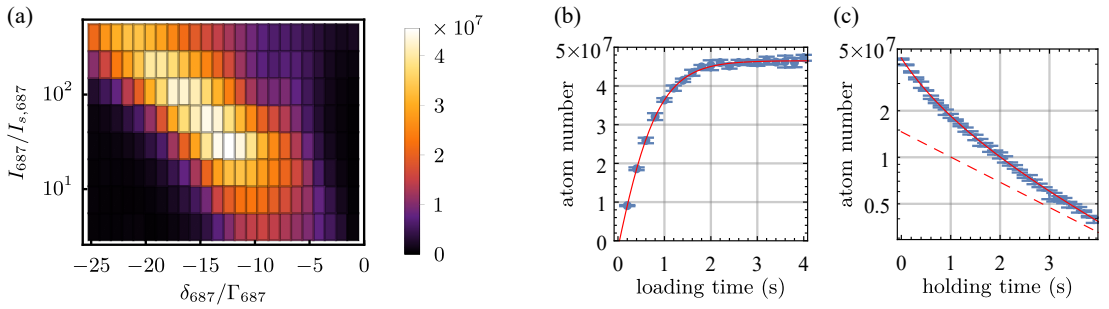

Figure 5.2: (a) The number of trapped atoms as a function of the detuning δ_{687} and the intensity I_{687}. The parameters for the yellow-MOT are fixed to the optimal conditions (see text). Loading (b) and decay (c) curves of the red-MOT under the optimal conditions. The solid lines are fitted to the data, and the dashed line in (c) is the exponential asymptote of the fit.

5.3 Spin composition

One of the features of a narrow-line MOT is the spontaneous spin polarization of the atoms in the MOT, as observed in the narrow-line MOTs of other lanthanide atoms [48,66]. As shown in Fig. 5.3, we evaluated the mean spin projection of the atoms in our red-MOT by using the Stern–Gerlach effect. After releasing the atoms from the red-MOT, we applied a 7-ms-long vertical magnetic field gradient of about 0.3 T/m. An absorption image was then obtained in the same manner as explained in Sec. 5.1. The typical absorption images are shown in Fig. 5.3 (a) and (b) along with the reference images, which were obtained without applying a magnetic field gradient. The populations of individual spin levels were estimated with multiple Gaussian fitting of the absorption images, considering the corresponding reference images. We estimated the population distributions as a function of the detuning δ_{687}, and calculated the mean spin projections $\langle F_z \rangle = \sum_{m_F=-6}^{6} p_{m_F} m_F$ from the obtained populations p_{m_F} as shown in Fig. 5.3(c). The figure reveals that atoms were well spin-polarized for larger detuning. With the detuning of $\delta_{687} = -21\,\Gamma_{687}$, 95 % of the atoms populated the lowest Zeeman sublevel $|F = 6, m_F = -6\rangle$.

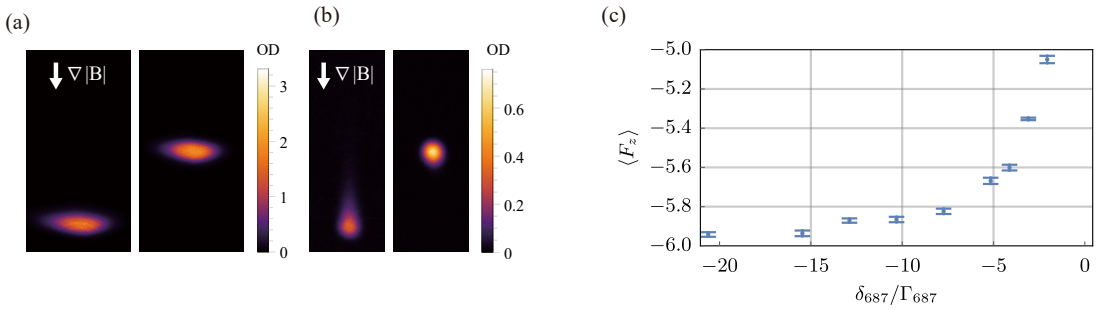

Figure 5.3: Spontaneous spin polarization in the narrow-line red-MOT. (a and b) Absorption images are taken at the same detuning of $\delta_{687} = -21\,\Gamma_{687}$ (a) and $\delta_{687} = -2\,\Gamma_{687}$ (b). The left images are taken after free expansion with applying a magnetic field gradient for spin separation, whereas the right images are taken in the absence of the magnetic field gradient. (c) The estimated mean spin projection $\langle F_z \rangle$ as a function of the detuning δ_{687}. The intensity is $I_{687} = 3\,I_{s,687}$, and the axial magnetic field gradient is $\partial B_z/\partial z = 3 \times 10^{-2}$ T/m.

5.4 Phase space density

To increase the phase space density of the atomic cloud, a compression sequence was performed after the loading stage. Using the optimal parameters $\partial B_z/\partial z = 2.5 \times 10^{-2}$ T/m, $I_{687} = 2\,I_{s,687}$, and $\delta_{687} = -6\,\Gamma_{687}$, we achieve a temperature of 6 μK and a peak number density of 2.2×10^{11} atoms/cm^3 with an atom number of 3.3×10^7. Under this condition, the population of $|F = 6, m_F = -6\rangle$ was inferred as about 0.8 from our Stern–Gerlach experiment, indicating a phase-space density of about 3×10^{-5}. The phase space density and the number of atoms after the compression stage provide us with good starting conditions for direct loading to an optical dipole trap.

5.5 Optical leak probability

We measured the transition probabilities for the leakage transitions from $z^{10}\mathrm{P}_{9/2}$ to $a^{10}\mathrm{D}^{\circ}_{7/2}$, $a^{10}\mathrm{D}^{\circ}_{9/2}$, and $a^{10}\mathrm{D}^{\circ}_{11/2}$. After loading the atoms, we turned off one of the three repumping beams, and kept an optical leak unplugged. Under this condition, the lifetime of the red-MOT is limited by the optical leak. By measuring the lifetime of the red-MOT, we estimated the transition probability for the unplugged leakage transition. In this manner, we measured the three transition probabilities, which are listed in Table 5.1.

upper level	lower level	λ (nm)	A_{ki} (s^{-1})
$z^{10}\mathrm{P}_{9/2}$	$a^{10}\mathrm{D}^{\circ}_{7/2}$	6602	$4.5(2) \times 10^3$
	$a^{10}\mathrm{D}^{\circ}_{9/2}$	7454	$7.4(2) \times 10^3$
	$a^{10}\mathrm{D}^{\circ}_{11/2}$	9039	$4.5(1) \times 10^3$

Table 5.1: The transition wavelengths λ and measured transition probabilities A_{ki} for the leakage transitions.

Chapter 6: Optical dipole trap for europium

Cold atom sample trapped in the red-MOT are loaded to an optical dipole trap (ODT), where they undergo evaporative cooling. It is the last step towards the creation of a a Bose-Einstein condensate. In this chapter I describe the optical dipole trap for europium.

6.1 Polarizability of europium

Optical dipole trap (ODT) is a conservative trap relying on the electric dipole interaction with far-detuned light. In the presence of a light field of frequency ω, the trapping potential $U(\omega)$ for atoms in Zeeman sublevel $|F, m_F\rangle$ is expressed as the sum of the scalar U_s, vector U_v, and tensor U_t parts as follows [67]:

$$U(r) = -\frac{1}{2\epsilon_0 c} I(r)\alpha_{tot} = U_s + U_v + U_t \tag{6.1}$$

$$U_s = -\frac{1}{2\epsilon_0 c} I(r) \cdot \alpha_s(\omega) \tag{6.2}$$

$$U_s = -\frac{1}{2\epsilon_0 c} I(r) \cdot \epsilon \cos\theta_k \frac{m_F}{2F} \cdot \alpha_v(\omega) \tag{6.3}$$

$$U_s = -\frac{1}{2\epsilon_0 c} I(r) \cdot \frac{3m_F^2 - F(F+1)}{F(2F-1)} \frac{3\cos^2\theta_p - 1}{2} \cdot \alpha_t(\omega) \tag{6.4}$$

where ϵ_0 is the vacuum permittivity; c is the speed of light; $I(r)$ it the laser intensity profile; $\epsilon = |\vec{u^*} \times \vec{u}|$ is the ellipticity parameter with $\vec{u}$ the normalized Jones vector; $\theta_p = \angle(\vec{E}, \vec{B})$ and $\theta_k = \angle(\vec{k}, \vec{B})$ (see Fig. 6.1); α_{tot} is the total atomic polarizability; $\alpha_s(\omega), \alpha_v(\omega), \alpha_t(\omega)$ are scalar, vector, and tensor dynamic polarizabilities, respectively.

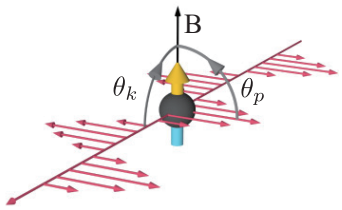

Figure 6.1: Schematic illustration of angles θ_k and θ_p. B denotes the orientation of the magnetic field. Reprinted from Ref. [68]

The dynamic dipole polarizability could be estimated with the sum-over state formula in Ref. [69, 70], which is summing contributions from each dipole transition to the polarizability. Every energy level and corresponding transition probability is required for the calculation. The polarizability for europium in the ground sate $F = 6$ hyperfine manifold is calculated based on this formula. We took account of 29 energy levels and corresponding transition probabilities taken from Ref. [51, 52, 71]. The result is shown in Fig. 6.2. One can see that vector and tensor polarizability are much smaller than scalar polarizability. It is a consequence of spherical electric orbital angular momentum of Eu in the ground state.

Low photon scattering rate is crucial to avoid heating or spin flip of atoms during

evaporative cooling. We also plotted photon scattering rates under a constant potential energy of 100 μK for atoms in $|F = 6, m_F = -6\rangle$ lowest Zeeman state with π polarization light[1]. One can see that laser light at a longer wavelength is more preferable for evaporative cooling.

In this experiment, We used a 1550 nm laser light for ODT beams. The polarizability and photon scattering rate are listed in Table 6.1.

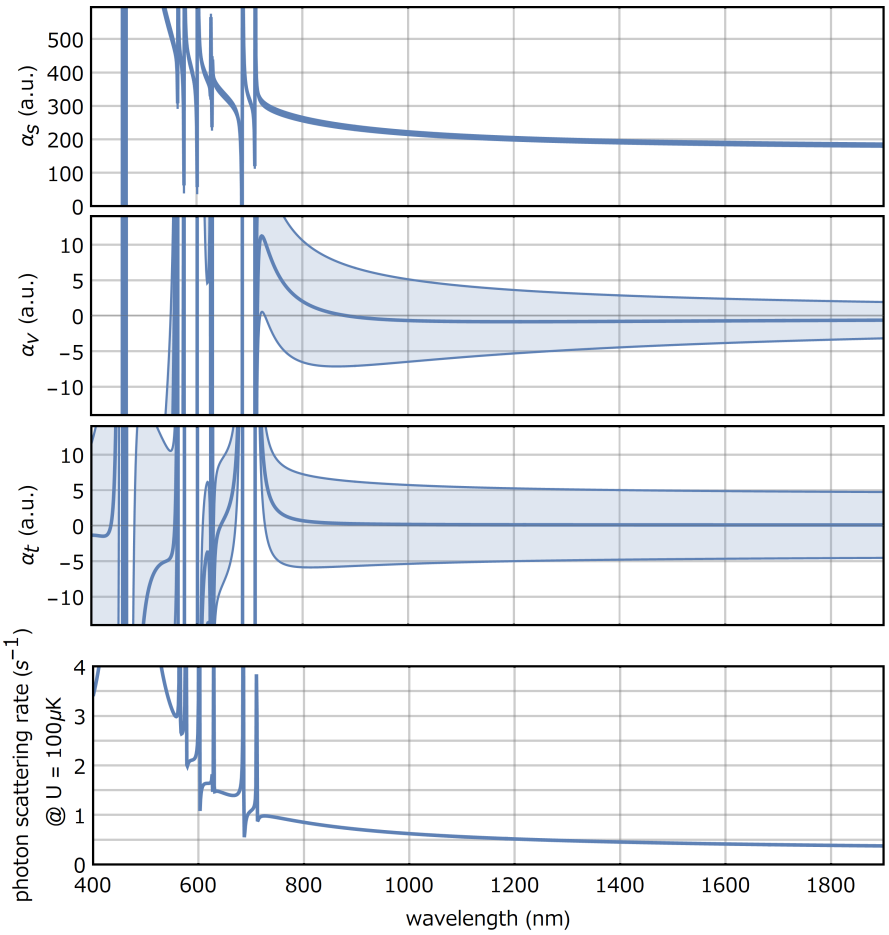

Figure 6.2: Scalar, vector, and tensor polarizability in the ground state as a function of the optical dipole trap wavelength. The shade region represents the uncertainty of the polarizabilities, which comes from uncertainties of the transition probabilities used in this calculation. The bottom figure shows photon scattering rate under a constant potential energy of 100 μK for atoms in $|F = 6, m_F = -6\rangle$ lowest Zeeman state with π polarization light.

[1] Although the photon scattering rate depends on Zeeman sublevel and polarization of light, their contribution is quite small since imaginary part of vector and tensor polarizability is also much smaller than scalar polarizability (within a few percentage of the scalar polarizability) except for near resonant wavelengths. It is in contrast to Er and Dy atoms [69, 72], which have large electric orbital angular momentum in their ground state.

Wavelength	α_s	α_v	α_t	photon scattering rate @ $U = 100\,\mu$K
1550 nm	189(5) a.u.	0(3) a.u.	0(5) a.u.	$0.43\,\mathrm{s}^{-1}$

Table 6.1: Scalar, vector and tensor polarizability for 1550 nm light. The polarizability is given in atomic units of $4\pi\epsilon_0 a_0^3$, where a_0 is the Bohr radius. The photon scattering rate under a potential energy of 100 μK is also listed.

6.2 Setup for an ODT

In ODT experiment for europium, we use 1550 nm laser with a maximum power of 15 W (see Sec. 4.2.7). We adopt crossed ODT geometry [73], whose setup is illustrated in Fig. 6.3. The trap consists of two crossing beams, a tightly confining horizontal beam and a less focused vertical beam. The beam parameters are summarized in Table 6.2.

The basic idea for evaporative cooling in the crossed ODT geometry is as follows. We first load atoms from red-MOT into horizontal ODT. In this condition atomic density is not sufficiently high to conduct evaporative cooling since confinement of the horizontal ODT along axial direction is quite week. Then, we add vertical ODT and gradually reduce power of horizontal ODT. Although almost atoms are initially trapped in the horizontal ODT and spread along axial direction, the atoms become concentrated into the crossed region as the horizontal ODT power decreases. Through this evaporative cooling procedure, we increase phase space density of an Eu atomic could and obtain a BEC.

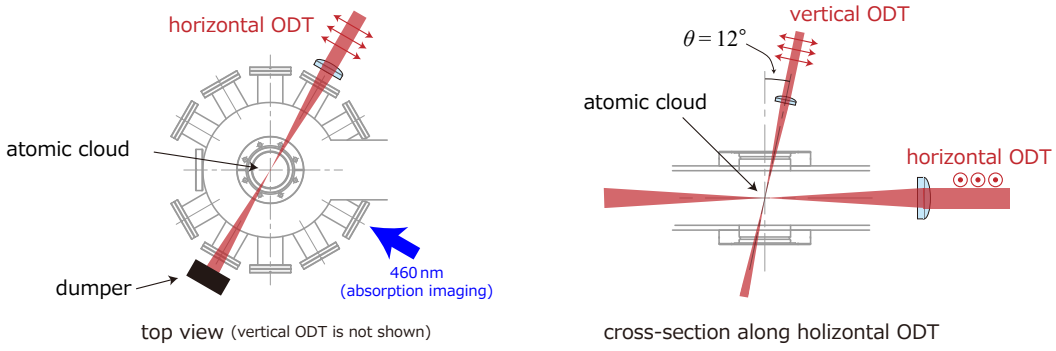

Figure 6.3: Setup for ODT.

6.3 Loading to an ODT

As described in previous section, we loaded atoms from the red-MOT to the horizontal ODT. After loading atoms to the red-MOT, we turned off laser lights that are not necessary for retaining red-MOT and blocked an atomic beam. Then we compressed red-MOT with following parameters: $\partial B_z/\partial z = 2\times10^{-2}\,\mathrm{T/m}$, $I_{687} = 0.8\,I_{s,687}$, and $\delta_{687} = -21\,\Gamma_{687}$. The compressed red-MOT contains 3×10^7 atoms with a temperature of $\sim 6\,\mu$K. Subsequently, we turned on the horizontal ODT beam with a power of 11.5 W, which overlaps the com-

	beam waist	maximum power	maximum potential depth
horizontal ODT	26 (30) μm	11.5 W	400 μK
vertical ODT	47 μm	7.4 W	90 μK

Table 6.2: List of ODT parameters. The beam waists are measured by Thorlabs' scanning-slit optical beam profiler BP209-IR/M. The beam profile of horizontal ODT has an elliptic cross section, where minor (major) axis is vertical (horizontal) direction. Note that the maximum power is available only when full power of the laser is assigned to one beam (see power recycling system in Sec. 4.2.7). Maximum potential depth is calculated based on the maximum power, the beam waist, and polarizability listed in Table 6.1.

pressed red-MOT. After 40 ms of loading, we obtained 1.4×10^6 atoms with a temperature of 50 μK in the horizontal ODT, whose absorption image is shown in Fig 6.4.

We note that the loading efficiency strongly depends on the polarization of the horizontal ODT beam. The successful loading was achieved with the horizontally polarized ODT beam, whereas we loaded only 2×10^5 atoms in the case of a vertically polarized ODT beam. The reason could be explained by differential tensor light shift for the 687 nm cooling transition, which is investigated in Sec. 6.4.

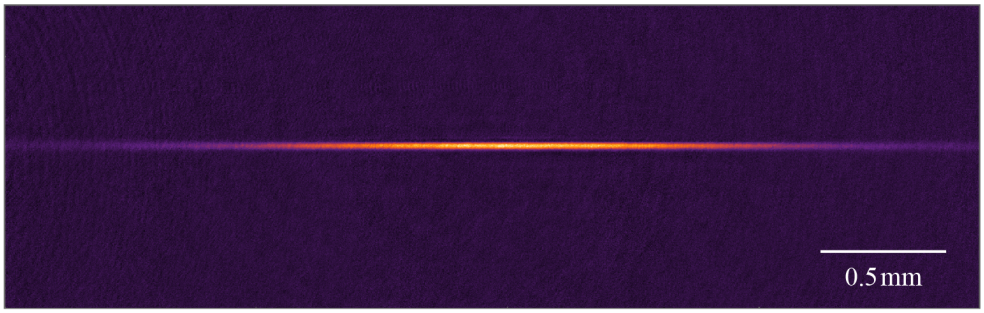

Figure 6.4: Absorption image after loading atoms to horizontal ODT

The loading efficiency from red-MOT to the ODT is only ~ 5 % at best. The low loading efficiency might be due to size mismatch between the horizontal ODT beam ($\sim$ 30 μm beam waist) and bowl-shaped compressed red-MOT ($\sim$ 2 mm diameter). Although one can increase the overlapping volume by expanding the ODT beam, which results in a reduction of the trap confinement force and less efficient evaporative cooling. One of the solution is a tunable trapping volume system using an AOM, which was introduced for other dipolar gas experiments [74–76]. Increasing loading efficiency will be a future task.

6.4 Differential light shift measurement

6.4.1 Differential light shift

Differential light shift is the difference between the light shifts for the exited state $U_e(r)$ and the ground state $U_g(r)$ in Eq. 6.1, which is represented as

$$\Delta U(r) = U_e(r) - U_g(r) \tag{6.5}$$

The differential light shift for the 687 nm cooling transition induced in the ODT is an important factor for loading atoms into the ODT. Figure 6.5 shows illustration of the energy in the case of positive and negative differential light shift. If the differential light shift is positive, red detuning of the cooling light is enhanced in the ODT, which may suppress light-assisted collisions induced by the cooling light. On the contrary, if the differential light shift is negative, detuning of the cooling light turns into blue in the ODT, which causes heating of atoms by the cooling light. If the differential tensor polarizability is comparable or larger than the scalar one, one can change the sign and magnitude of the differential light shift by rotating polarization of the ODT beam or direction of the bias magnetic field. It can be utilized to optimize the efficiency of Doppler cooling for atomic gas in an ODT [77].

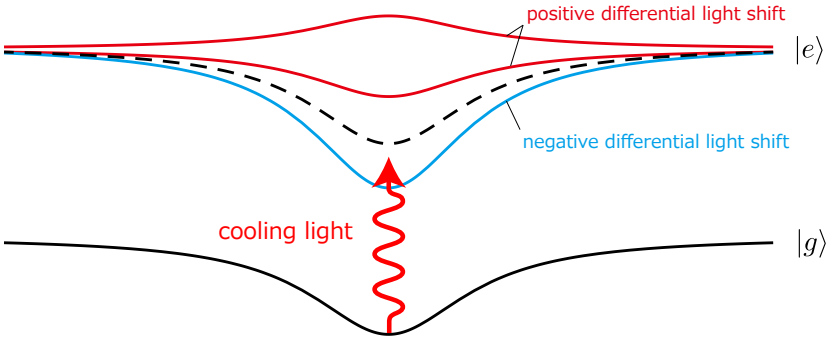

Figure 6.5: Illustration of the energy of atoms in an ODT with Gaussian shape. The excited levels for positive (negative) differential light shift are drawn by red (blue) line. The upper (lower) red line indicates energy in the case of the excited-state polarizability negative (positive).

Unfortunately, we cannot estimate the excited-state polarizability by using sum-over state formula since information of the transition probabilities relevant to the $z^{10}\mathrm{P}_{9/2}$ exited state are lacking significantly. Hence, we measured the light shift experimentally.

6.4.2 Differential light shift measurement

In this work, we measured differential light shift for the $|F = 6, m_F = -6\rangle \leftrightarrow |F' = 7, m_{F'} = -7\rangle$ transition induced by a linearly polarized ODT beam. Under the condition, differential light shift is written as

$$\Delta U(r) = -\frac{1}{2\epsilon_0 c} I(r) \left(\Delta\alpha_s + \frac{3\cos^2\theta_p - 1}{2} \cdot \Delta\alpha_t \right) \tag{6.6}$$

where $\Delta\alpha_s$ and $\Delta\alpha_t$ are the scalar and tensor polarizability differences between in the ground and exited state, respectively. By measuring the differential light shift for various values of θ_p, we can characterize the differential light shift.

In order to measure the resonant frequency, we utilized the large optical leaks from the $z^{10}\mathrm{P}_{9/2}$ exited state to metastable states (see Sec. 5.5). We applied a 687 nm probe light to the atoms. If the frequency of the probe light matches the energy difference between

the ground and the excited state, we can find a resonant atom loss since atoms leak to the metastable state.

Our measurement start from an atomic sample polarized to $|F = 6, m_F = -6\rangle$ Zeeman state, trapped in the ODT. The relative angle θ_p was set by changing direction of the bias magnetic field, whose amplitude was $0.5 \sim 2\,\mathrm{G}$. Then we applied a probe beam for 2 ms, whose polarization was σ_-[2] and intensity of $1 \cdot I_{s,687}$. The ODT was then switched off and an absorption image was taken to measure the remained number of atoms. By scanning the frequency of the probe light, we extracted the resonance frequency. The resonant frequency with no light shift was also extracted from a similar resonance measurement, where the probe light was applied after switching off the OTD beam. By comparing the two resonant frequencies, we can obtain the differential light shift.

Figure 6.6 (a-c) shows the atom loss spectra with $\theta_p = 0°,\ 60°$, and $90°$, respectively. The upper (lower) panels show number of atoms in the absence of the trap (in the trap). The resonant frequency for atoms in the absence of trap is determined by fitting data with Lorentzian function. On the other hand, the atom loss spectra for atoms in the trap are obviously broaden in the case of $\theta_p = 0°$ and $60°$. It can be explained by atomic distribution in the trap. Since atomic temperature in the trap over the potential depth is only $\sim 1/5$ in this experiment, atoms were distributed from the bottom to the edge of the trap, which broadens the atom loss spectra. Since there is no reliable fitting function, we regarded the frequency where the most atoms seem to loss as the resonant frequency. Both resonant frequencies are indicated by the vertical dotted line and light shifts are extracted from the frequency differences.

Although light shift was determined roughly, we can capture the characteristic of the light shift. The measured light shifts are plotted in Fig. 6.6 (d) as a function of θ_p and fitted by Eq. 6.6. One can see that the light shift are negative in most regions of θ_p. This θ_p dependence of the differential light shift can explain the dependence of the loading efficiency on the the polarization of the ODT beam in Sec. 6.3. Since the compressed red-MOT position drop due to the gravity, magnetic field direction at the MOT position is vertical. Under the condition, vertical polarization of the ODT corresponds to $\theta_p = 0°$. The negative light shift induces heating of atoms by the cooling light, which may result in low loading efficiency. On the contrary, the horizontal polarization of the ODT beam corresponds to $\theta_p = 90°$. The light shift is almost zero at the polarization, which may results in lower heating and higher loading efficiency compared in the case of the vertically polarized ODT beam.

[2] In the case of $\theta_p = 90°$, we used a probe beam that is linearly polarized in the direction perpendicular to the bias magnetic field. Although it contains both σ_+ and σ_- polarization component, Zeeman splitting is much larger than the light shift. Therefore σ_+ polarization component dose not affect this measurement.

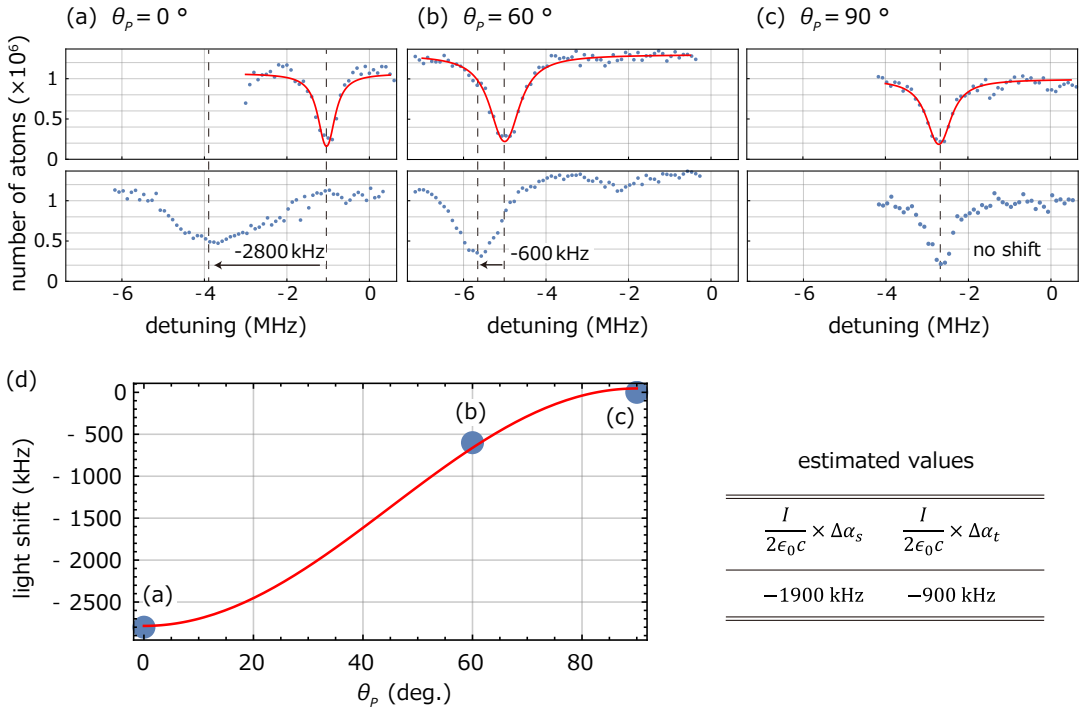

Figure 6.6: (a), (b), and (c) Remained number of atoms as a function of probe light detuning with $\theta_p = 0°$, 60°, and 90°, respectively. The upper panels are for atoms in the absence of the trap, whereas the lower panels are for atoms in the trap. (d) The measured light shifts are plotted as a function of θ_p. The red line is a fit based on Eq. 6.6. The estimated parameters are listed in the right table.

7.1 Creation of a Eu BEC

7.1.1 Evaporative cooling

To obtain a BEC, we have to increase phase space density (PSD) of trapped atoms, which is defined as

$$\mathrm{PSD} = n_0 \lambda_{dB}^3 \tag{7.1}$$

where n_0 is the peak number density of the gas, $\lambda_{dB} = h/\sqrt{2\pi m k_B T}$ is the thermal de Broglie wavelength, m is the atomic mass of Eu, k_B is the Boltzmann constant, and T is the temperature of the trapped atoms. Both high atom number density and low temperature are required for high PSD. The phase transition to BEC occurs when the PSD reaches to 2.6 [78], where the thermal de Broglie wavelength is on the order of the interparticle distance.

As described in Sec. 6.3, initial condition just after loading to horizontal ODT is 1.4×10^6 atoms at a temperature of 50 μK, which corresponds to a PSD of only 5×10^{-6}. We increased the PSD with evaporative cooling technique. We gradually decreased the trap depth and let the most energetic atoms in the trap escape over the potential barrier. The evaporative cooling was achieved in the following sequence. After loading atoms to the horizontal ODT, we tuned off the red-MOT beams and the quadrupole magnetic field. Then, we switched on a homogeneous magnetic field of 1.1 G along the horizontal ODT beam to preserve the spin polarization of the sample. Subsequently, we gradually decreased horizontal ODT power and increase the vertical ODT power, as described in Fig. 7.1. This operation concentrated atoms into the crossed region and increased atom number density; almost all atoms were trapped in the crossed region at the evaporation time of 6 s. After 7.4 s evaporative cooling we produced an almost pure BEC with 3×10^3 atoms, which is described in the next section.

Note that the BEC was obtained only when the polarization of the vODT was orthogonal to that of the hODT. When the polarization of the vODT was parallel, atoms seems to be heated even though the frequencies of the two trapping beam differs 160 MHz. Further investigation is required to clarify the cause of the polarization dependence.

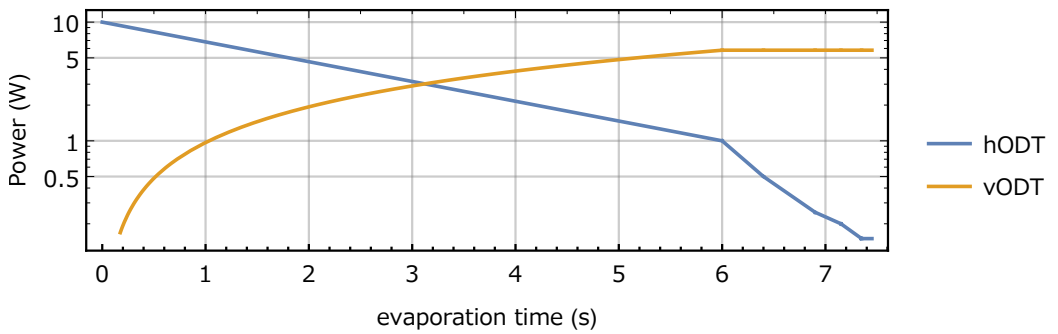

Figure 7.1: Crossed ODT beam power trajectory during evaporative cooling.

7.1.2 First observation of a Eu BEC

Figure 7.2 shows the absorption images taken after 13 ms of expansion for different final temperature. At higher temperature (a) the atomic distribution is well described by Maxwell-Boltzmann distribution. By cooling the atoms below the critical temperature, we observed a clear bimodal profile (b). The characteristic shape was one of the key evidence for BEC. At lower temperature, we observed almost pure condensate with 3×10^3 atoms (c). The slightly tilting elliptic shape of the condensate reflects the vODT beam crossed to hODT with an angle of 78 °, which is illustrated in the absorption image (c).

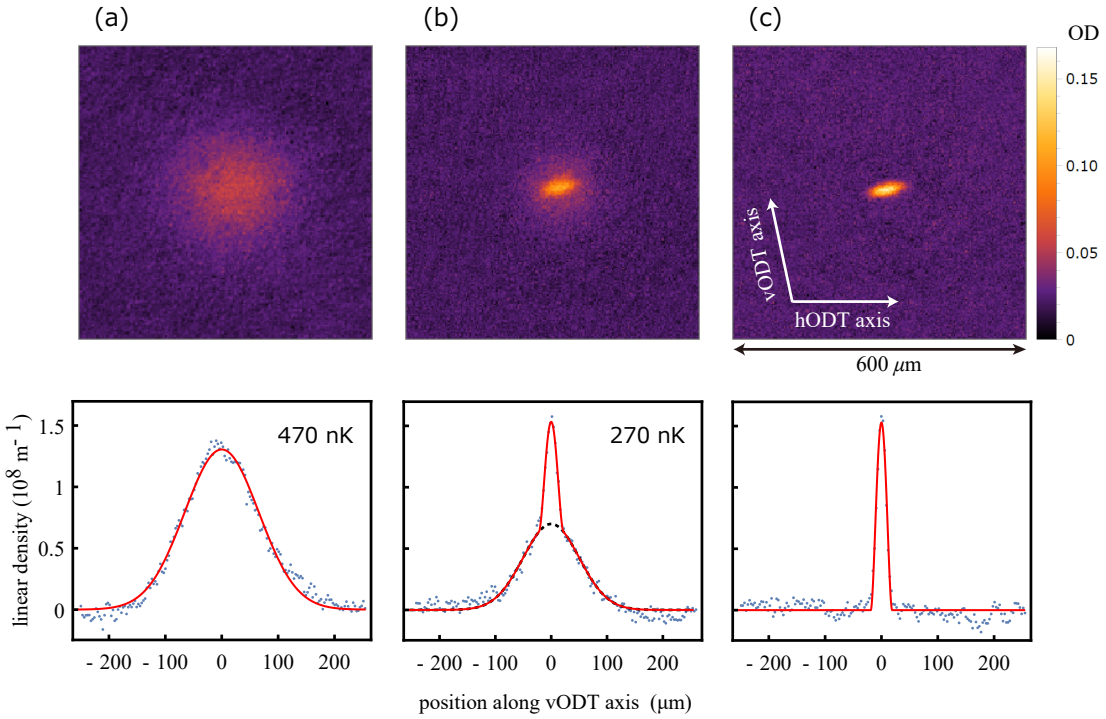

Figure 7.2: (Top) Absorption images showing the BEC phase transition for different final hODT power. The absorption images are an average of five images taken after 13 ms of expansion. (Bottom) Integrated linear profiles along direction orthogonal to vODT axis. The solid lines are fit to the data using Gaussian (a), bimodal (b), and Thomas-Fermi (c) distribution. The dotted lines represent the Gaussian part of the bimodal fit. From the fit we extract: $N = 2.2 \times 10^4, T = 470\,\text{nK}$ (a), $N = 1.1 \times 10^4, T = 270\,\text{nK}$ (b), and $N = 3 \times 10^3$ (c), where N is the total atom number.

To confirm the validity of the phase transition, we calculated a critical temperature. The critical temperature is given by the following equation: [79]

$$T_C^0 = \frac{\hbar\bar{\omega}}{k_B}\left(\frac{N}{\xi(3)}\right)^{\frac{1}{3}} \simeq 0.94\frac{\hbar\bar{\omega}}{k_B}N^{\frac{1}{3}} \tag{7.2}$$

Here, $\bar{\omega}$ is the geometric mean trap frequency, which we extracted from ODT beam waists and power, and polarizability calculated in Sec. 6.1. When finite size effects as well as a correction arising from the contact interaction [79] are taken into account, the critical

temperature is shifted to lower temperatures:

$$T_C^* = T_C^0 + \delta T_C^{fs} + \delta T_C^{int} \tag{7.3}$$

where $\delta T_C^{fs} \simeq -0.73 \frac{\langle\omega\rangle}{\bar{\omega}} N^{-\frac{1}{3}} T_C^0$ is a shift due to the finite number of atoms and $\delta T_C^{int} \simeq -1.33 \frac{a_s}{a_{HO}} N^{\frac{1}{6}} T_C^0$ is a shift due to contact interaction. Here $\langle\omega\rangle$ is the arithmetic mean trap frequency, a_s is the s-wave scattering length, $a_{HO} = \sqrt{\frac{\hbar}{m\bar{\omega}}}$ is the length of the harmonic oscillator corresponding to the trap. We set $a_s = 135\, a_B$, that is measured in Sec. 7.2.3. By using aforementioned equations, we obtain $T/T_C^* = 1.14$ (a) and $T/T_C^* = 0.86$ (b), which are consistent with our observation.

7.1.3 Optimization of the evaporative cooling

After observation of the BEC, we optimized the evaporative cooling process, increasing a number of condensed atoms to 1.5×10^4. The key ingredients for the improvement were loosening vODT confinement in the last stage of the evaporative cooling, and setting the bias magnetic field to 3.0 G during the evaporative cooling. Figure 7.3 shows improved crossed ODT beam power trajectory. The power of vODT was reduced to 1/4 in the last stage of the evaporative cooling, which reduces three-body inelastic collision.

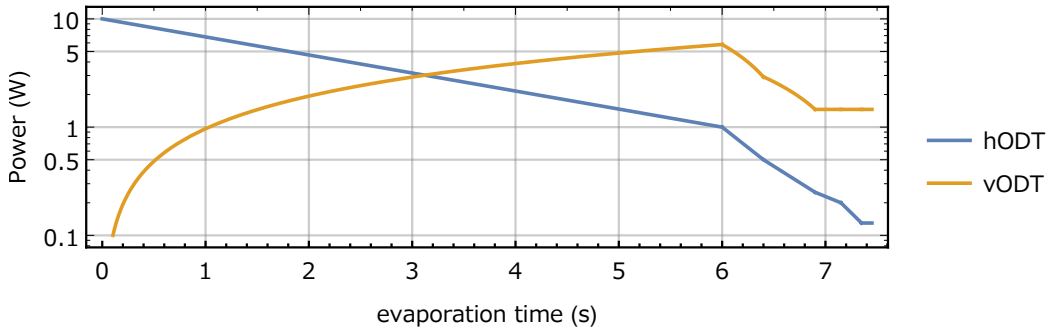

Figure 7.3: Improved crossed ODT beam power trajectory during evaporative cooling.

A value of the bias magnetic field is also important for efficient evaporative cooling in the case of Eu. Figure 7.4 shows number of atoms after evaporative cooling as a function of bias magnetic field during the evaporative cooling. Here the magnetic field was oriented to vertical direction and almost all atoms were condensed at the magnetic field where larger number of atoms were remained. One can see clear dependence of the remained atoms on the bias magnetic field. It would be due to inelastic collisional loss induced by Feshbach resonances. Maximum number of atoms was obtained around a magnetic field of 3.0 G.

The evaporative cooling efficiency is often evaluated by using the following formula [80]:

$$\gamma = -\frac{\ln(\rho_f/\rho_i)}{\ln(N_f/N_i)} \tag{7.4}$$

where ρ_i, ρ_f are the initial and final PSD, and N_i, N_f are the initial and final number of atoms. The γ represents the order of magnitude increase of the PSD at the expense of an order of magnitude of atom number. By using this formula, overall efficiency of our

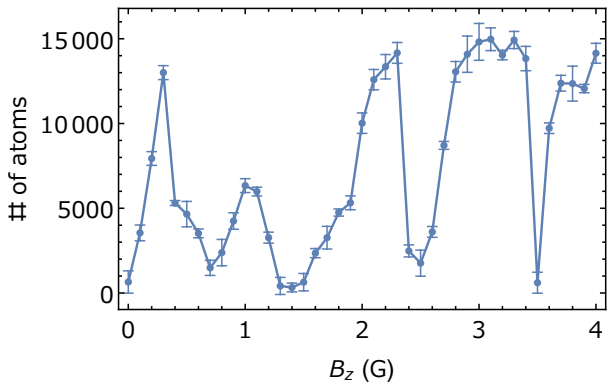

Figure 7.4: Number of atoms after evaporative cooling as a function of bias magnetic field.

evaporative cooling process was evaluated to be $\gamma = 3.6$, which is a good value considering many other experiments typically achieve values of $\gamma \approx 2.5 \sim 3.5$ [80].

7.1.4 Lifetime of the BEC

The lifetime of the BEC in the trap is of interest since one can manipulate or develop the BEC within the time. We measured the number of atoms as a function of the holding time after creating the BEC, which is shown in Fig. 7.5. The data was fitted using a three-body and one-body loss model for a three dimensional BEC [81]:

$$\frac{dN}{dt} = -\gamma N^{9/5} - \alpha N \tag{7.5}$$

whose solution is given by:

$$N(t) = \left[\left(N_0^{-4/5} + \frac{\gamma}{\alpha}\right) e^{\frac{4}{5}\alpha t} - \frac{\gamma}{\alpha}\right]^{-5/4} \tag{7.6}$$

The data was described by only three-body loss, and we couldn't estimate one-body loss rate α. A $1/e$ lifetime for the initial three-body loss is estimated to $\left(\gamma N^{4/5}\right)^{-1} = 1.4\,\mathrm{s}$. Corresponding three-body loss coefficient can be obtained by the following [81]:

$$L = \gamma \frac{6}{7} \left((15^{2/5}/(14\pi))(m\bar{\omega}/(\hbar\sqrt{a_s}))^{6/5}\right)^{-2} \tag{7.7}$$

By using $a_s = 135\,a_B$ and $\bar{\omega} = 2\pi \times 204\,\mathrm{Hz}$, we extract $L \sim 10^{-41}\,\mathrm{cm}^6/\mathrm{s}$, which is the same order of that for rubidium atom in $|F = 2, m_F = 2\rangle$ [81].

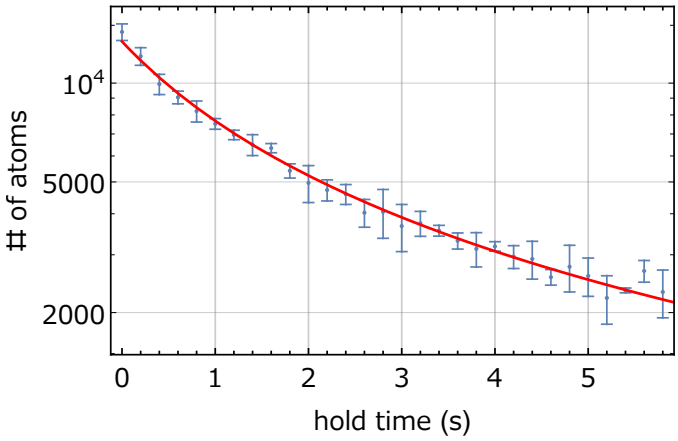

Figure 7.5: Number of atoms as a function of hold time. The red line is a fit to the data with the Eq. 7.6.

7.2 Dipolar effect in a Eu BEC

The DDI effect in a BEC can be observed as anisotropic deformation of the expanding BEC, which was first observed in a ^{52}Cr BEC [82] in 2005. In this section, I start with a short summary of the theoretical description of DDI in a BEC. Then I compare the theory and experimental result.

7.2.1 Theoretical description

Description of dipolar BEC was well understood when DDI is smaller than s-wave contact interaction ($\epsilon_{dd} < 1$ regime, see Eq. 7.12). The theory of the dipolar BEC was confirmed with experimental results in the expansion dynamics of a dipolar ^{52}Cr BEC by the group of T. Pfau in Stuttgart [4,8,82,83]. (Their results were also summarized in PhD theses [84,85], PhD tutorial [86], and a review article [87].) In the following, I will describe short summary of the dipolar BEC theory in a harmonic trap. Most of this section is quoted from Ref. [83] (S. Giovanazzi, PRA **74**, 013621 (2006)).

Gross-Pitaevskii equation of a dipolar BEC

The generalized time-dependent Gross-Pitaevskii equation is given by

$$i\hbar\frac{\partial}{\partial t}\Psi(\vec{r},t) = -\frac{\hbar^2}{2m}\nabla^2\Psi(\vec{r},t) + V_{\text{ext}}(\vec{r},t)\Psi(\vec{r},t) + V_{\text{mf}}(\vec{r},t)\Psi(\vec{r},t) \tag{7.8}$$

where V_{ext} is an external potential and V_{mf} is the mean-field potential given by

$$V_{\text{mf}} = gn(\vec{r},t) + \int d^3r' U_{dd}(\vec{r}-\vec{r'})n(\vec{r'},t) \tag{7.9}$$

where $n(\vec{r'},t) = |\Psi(\vec{r},t)|^2$ is the condensate atomic density and m is the atomic mass. In Eq. 7.9 g is the s-wave scattering coupling constant given by

$$g = \frac{4\pi\hbar^2 a_s}{m} \tag{7.10}$$

where a_s is the s-wave scattering length. Here

$$U_{dd}(\vec{r}) = \frac{\mu_0 \mu_m^2}{4\pi r^3}\left(1 - \frac{3(\hat{e_\mu}\,\vec{r})}{r^2}\right) \tag{7.11}$$

is the DDI energy between two equally oriented magnetic dipole $\vec{\mu_m} = \mu_m \hat{e_\mu}$ aligned by a polarizing magnetic field. Here, we introduce a measure of the strength of the DDI relative to the s-wave scattering energy:

$$\epsilon_{dd} = \frac{\mu_0 \mu_m^2 m}{12\pi\hbar^2 a_s} \tag{7.12}$$

If $\epsilon_{dd} > 1$, instabilities can occur in the hydrodynamic limit. Dipolar BECs with $\epsilon_{dd} > 1$ are recently enthusiastically investigated by using BEC of chromium and dipolar lanthanide atoms: erbium and dysprosium. Many fascinating phenomena such as d-wave collapse, Rosensweig instability, roton excitation, super solid phase were observed. On the other hand, if $\epsilon_{dd} < 1$, the GP equation has a stable solution, which we consider in the following.

Solutions in the Thomas-Fermi limit for harmonic potential

It is worth noting that although DDI has the nonlocal character, we shall obtain inverted parabola density profile, which is equivalent to the results obtained for ordinary nondipolar BECs. In the Thomas-Fermi limit, the solution of the Eq. 7.8 for time-dependent harmonic trap is given by [83, 88]

$$n(\vec{r}, t) = \frac{15N}{8\pi R_x R_y R_z}\left[1 - \frac{x^2}{R_x^2} - \frac{y^2}{R_y^2} - \frac{z^2}{R_z^2}\right] \tag{7.13}$$

$$\vec{v}(\vec{r}, t) = \frac{1}{2}\vec{\nabla}[\alpha_x x^2 + \alpha_y y^2 + \alpha_z z^2] \tag{7.14}$$

The density $n(\vec{r}, t)$ and the velocity field $\vec{v}(\vec{r}, t)$ depend on time only though the time dependence of the condensate radii $R_j(t)$ and the $\alpha_j(t)$ coefficients. The latter are simply given by

$$\alpha_j(t) = \frac{\partial}{\partial t}\ln[R_j(t)] \tag{7.15}$$

By using the result, one can easily solve the GP equation 7.8 for equilibrium configuration in a harmonic trap and expansion dynamics, which we are now interested in.

General trend of a dipolar BEC

By solving the equation, one can extract the effect of the DDI to the condensate, which was analytically studied in detail in Ref. [83]. General trend of the dipolar BEC was schematically drawn in Fig. 7.6. The dipolar BEC tends to have a shape elongated in the direction of the magnetic field both in trap and after expansion.

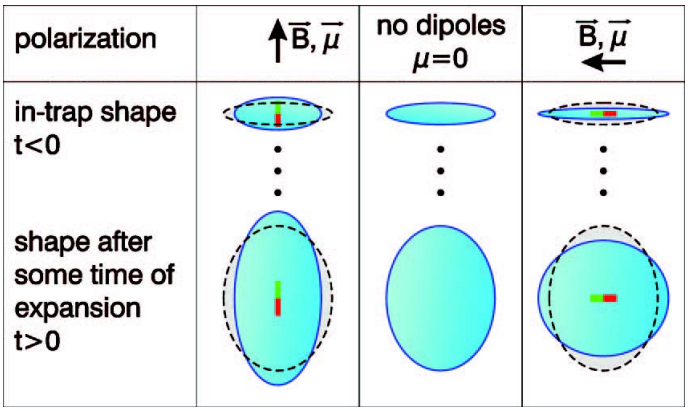

Figure 7.6: *Figure to illustrate the change of the condensate shape under the influence of magnetization in trap (top row) and during time of flight (bottom row). Left column, magnetization in transversal direction; center column, nondipolar atoms; right column, longitudinal polarization. Dashed ellipses represent the nondipolar condensate.* Reprinted from Ref. [83].

7.2.2 Observation of dipole-dipole interaction in a BEC

As described in the previous section, DDI effect can be observed as an anisotropic deformation of the expanding BEC. To confirm the DDI effect of the Eu BEC, we took two absorption images of BECs that were released under a bias magnetic field of 1.5 G oriented to vertical and horizontal direction. The images are shown in Fig. 7.7. One can see that the shape of the expanding BEC is clearly elongated to the direction of the magnetic field. It is a clear evidence that Eu BEC is a strongly dipolar BEC. The ratio between the width of the minor axis in (a) and (b) reaches to 1.25.

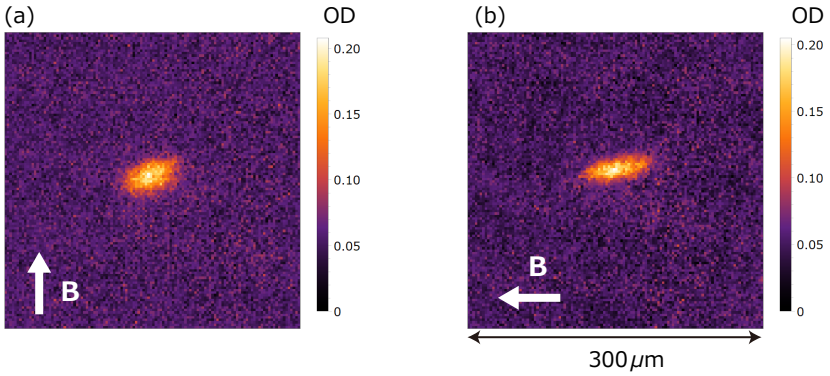

Figure 7.7: Absorption images of a BEC taken after 13 ms of expansion. The image shows the BEC that was released under a bias magnetic field of 1.5 G oriented to vertical (a) and horizontal (b) direction. White arrows indicate the magnetic field direction.

7.2.3 Estimation of s-wave scattering length

The s-wave scattering length is a crucial parameter that characterizes the BEC. A simple method to measure the s-wave scattering length is to estimate the scattering length from an expansion speed of the BEC [73, 89]. This method is also applicable for dipolar

BEC [4]. However, the estimation often accompanies large errors due to error of number of atoms or expansion speed.

Axel Griesmaier proposed and demonstrated a simple and more accurate method to estimate the s-wave scattering length in dipolar BEC [4] . He measured asymptotic velocities of expansion of the ^{52}Cr condensate with different orientation of the atomic magnetic moment. Then, he compared the ratio of the velocities to the numerical simulation of the expanding dipolar BEC and got a relative DDI strength ϵ_{dd} and corresponding s-wave scattering length. The values was in excellent agreement with the s-wave scattering length that has been obtained by comparing the measured positions of Feshbach resonance in chromium collisions with multichannel calculations [90].

Here we use the same method to estimate s-wave scattering length. In the previous section, we already got a experimental result on the ratio of the velocities of 1.25. By comparing the ratio to the numerical solution, we get a $\epsilon_{dd} = 0.44$, which corresponds to a s-wave scattering length of $a_s = 135\,a_B$. Note that the magnetic field direction is slightly tilted to the ODT trapping axis ($\sim 12°$), which I did not take into account to the calculation. More proper estimation is a future task.

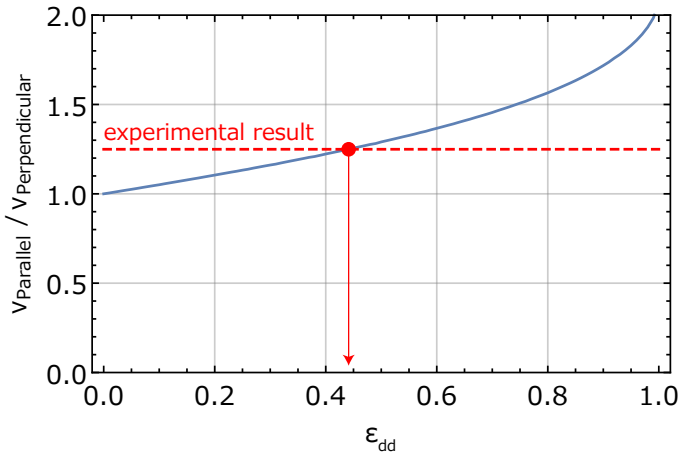

Figure 7.8: Estimation of the s-wave scattering length for ^{151}Eu. The solid blue line is a numerical simulation of the ratio of the expanding velocities when the magnetic field was set to parallel and perpendicular to the velocity axis, as a function of ϵ_{dd}. Dashed red line indicates experimental result. From the crossing point of the experimental result and numerical simulation, we extracted a relative DDI strength of $\epsilon_{dd} = 0.44$.

7.3 Feshbach resonance

Feshbach resonance is a powerful tool to control the interaction between ultracold atoms [91]. The experiment on Feshbach resonance is currently in progress. In this section, I will present some preliminary results of the Feshbach spectroscopy for Eu atoms.

7.3.1 Feshbach spectroscopy ($0 \sim 4$ G)

In the optimization of the evaporative cooling in Sec. 7.1.3, we observed that evaporative cooling efficiency depends on a value of bias magnetic field, which suggests there are

some Feshbach resonances in low magnetic field region. Our interest is whether these Feshbach resonances can be used to control the s-wave scattering length or not. As reported in Feshbach spectroscopy experiments of other dipolar atoms, some resonances of the dipolar atoms have strong temperature dependence [30, 32, 33, 92, 93]. Feshbach resonances with nonzero partial-wave entrance channels were observed only at high temperature and vanished at lower temperature [30, 33]. These resonances cannot be used to control s-wave scattering length in BEC experiments.

To investigate the Feshbach resonances of Eu, we conducted Feshbach spectroscopy for a Eu BEC. After creating a BEC at a magnetic field of $B_z = 1.0\,\mathrm{G}$, we changed the magnetic field to the desired value and hold 100 ms. Then we released the BEC from the ODT and measured remaining number of atoms, which are plotted in Fig. 7.9 (b). Figure 7.9 (a) is the copy of Fig 7.4 for a reference. Note that this spectroscopy was conducted before we optimized evaporative cooling, resulting in lower number of atoms. From this result, one can see one broad resonance at 1.3 G and one narrow resonance at 3.4 G, whereas the other resonances observed in (a) vanished. The relatively broad Feshbach resonance at 1.3 G might be used to control the s-wave scattering length.

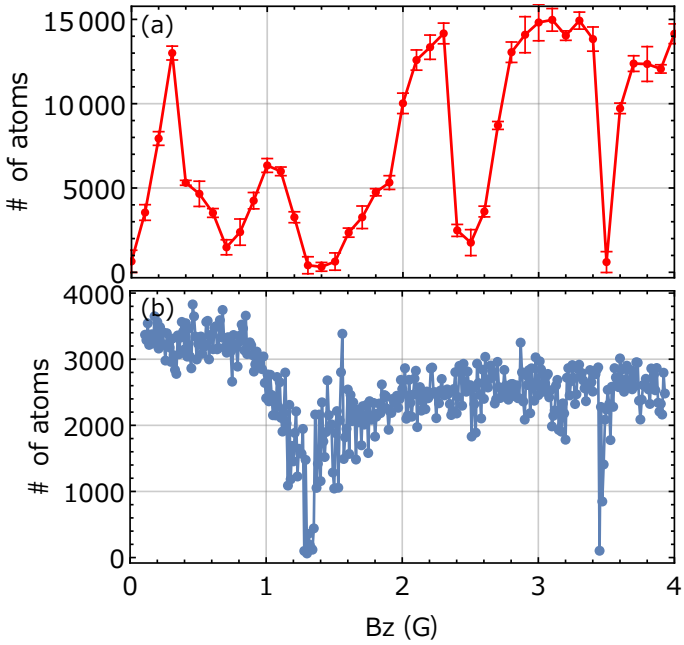

Figure 7.9: Feshbach spectroscopy below 4 G. (a) Copy of Fig. 7.4 for a reference. Number of atoms after 7.5 s evaporative cooling were plotted. The initial temperature was $\sim 50\,\mu$K. (b) Remaining number of atoms after 100 ms holding time at a magnetic field B_z. The magnetic field resolution is 10 mG.

In order to investigate the tunability of the s-wave scattering length, we conducted the following experiment. After creating a BEC at a magnetic field of $B_z = 3.0\,\mathrm{G}$, we changed the magnetic field to 1.5 G, which is ~ 200 mG above the resonance. Then, we linearly ramped down the magnetic field to a target value within 2 ms and hold atoms 1 ms at the magnetic field and switched off the ODT. After free expansion of 13 ms, we took an absorption image. The absorption images for different target magnetic field are listed in

Fig. 7.10. One can see a clear change of the aspect ratio at the vicinity of the resonance. The change of the aspect ratio implies a change of ϵ_{dd}, which indicates a change of the s-wave scattering length. The remaining number of atoms and aspect ratio are shown in Fig. 7.11.

In future work, we will investigate the Feshbach resonance in details including, lifetime at the vicinity of the resonance, temperature dependence, resonance width, and determining the s-wave scattering length as a function of the magnetic field.

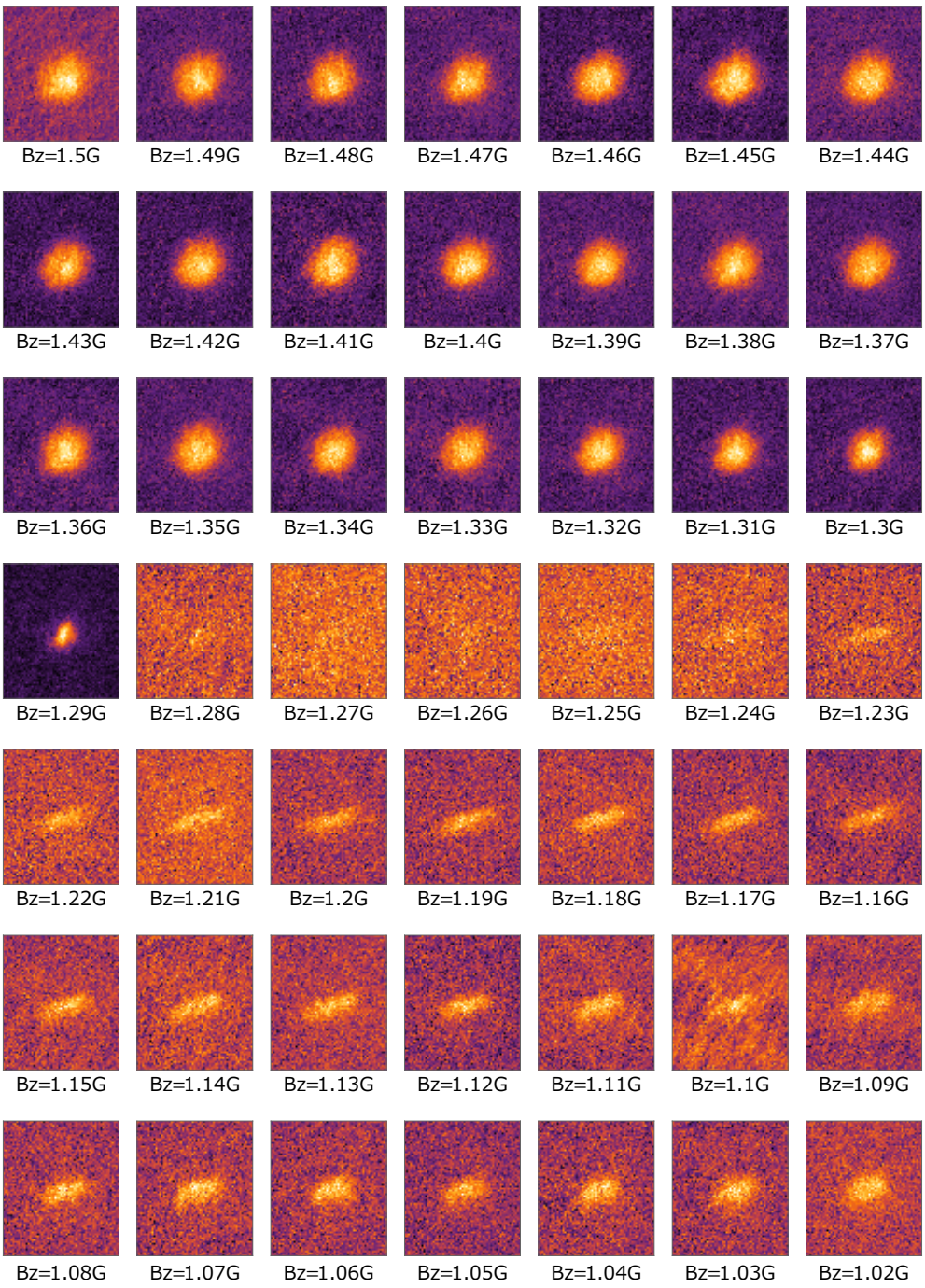

Figure 7.10: Absorption images of a BEC taken after holding the BEC at the magnetic field B_z and free expansion of 13 ms.

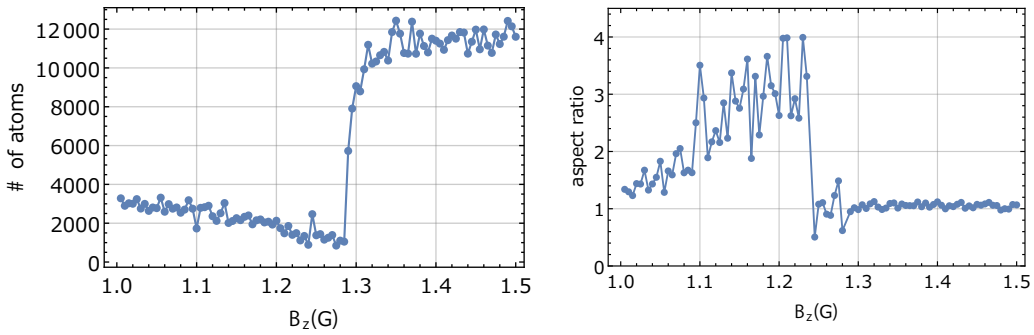

Figure 7.11: Remaining number of atoms (left) and aspect ratio of the BEC (right) as a function of B_z.

7.3.2 Preliminary measurement for Feshbach spectroscopy (0∼34 G)

Feshbach spectroscopy for higher magnetic field is of interest in the following point. Feshbach resonance of other lanthanide atoms (Dy, Er, and Tm) shows very dense Feshbach spectrum, whose nearest-neighbor spacings has chaotic statics [30, 31, 33]. In theoretical analysis, the reason of the chaotic character is expected to be their large electronic orbital angular momentum. On the other hand, Feshbach spectrum of Eu is expected to be not so dense and non chaotic character since Eu has zero electronic orbital angular momentum [34]. It is interesting to confirm whether Feshbach spectrum of Eu is dense and chaotic or not.

In addition, if the Feshbach spectrum of Eu is sparse and not chaotic as expected by the theory, one may be able to determine molecular potential by comparing resonance positions with multichannel scattering calculations [90, 94]. The result can be used to determine the s-wave scattering length precisely for all combination of the total spin. These values are essential for spinor dipolar BEC experiment. Moreover, the molecular potential may be useful for searching weakly bound state available for RF Feshbach resonance, which we initially planed to use for spinor dipolar BEC experiment.

For the above purpose, we conducted the following evaporative cooling measurement. We measured remained number of atoms after evaporative cooling at various bias magnetic field with a resolution of 100 mG and a maximum magnetic field below a magnetic field of 34 G. This measurement enable us to easily detect narrow resonances such as a resonance at 3.4 G in Fig. 7.9 (b) or resonances with nonzero partial-wave entrance channels such as a resonance at 2.5 G in Fig. 7.9 (a). The experimental result is shown in Fig. 7.12. One can see about 25 resonances within 34 G, which is less dense than those of other dipolar atoms ($3 \sim 26\,\mathrm{G}^{-1}$). In future, we will conduct Feshbach spectroscopy in smaller magnetic field resolution at lower temperature to identify whether these observed resonances remain at the lower temperature or not and Feshbach spectrum of Eu is chaotic or not.

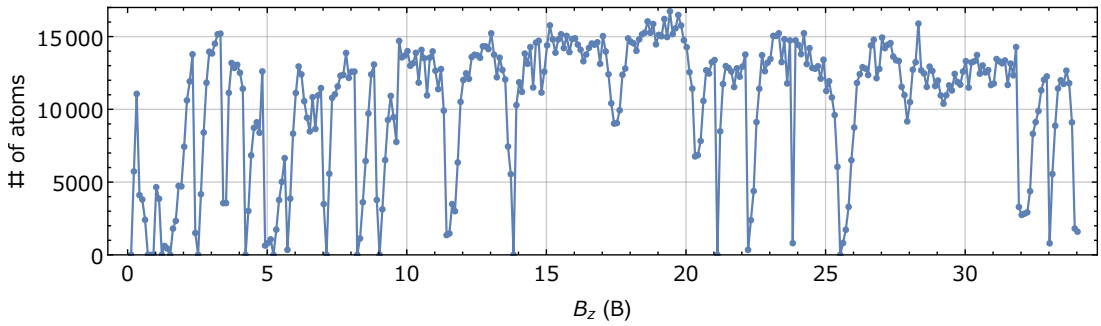

Figure 7.12: Remaining number of atoms after evaporative cooling procedure under a bias magnetic field of B_z. The initial temperature was $\sim 50\,\mu$K. The magnetic field resolution was 100 mG.

Chapter 8: Conclusion and outlook

8.1 Summary

Europium is a promising candidate for exploring rich ground-state phases of dipolar BEC under ultra-low magnetic field, since Eu has both large dipole moment of $7\mu_B$ and hyperfine structure.

In this thesis, I described the creation of a BEC of ^{151}Eu. Since Eu had not been laser-cooled yet when we started to laser-cool Eu atom, many crucial parameters to cool atoms were unknown, such as optical leak probabilities, polarizabilities, and s-wave scattering length. Nevertheless, we successfully produced a Eu BEC with an atom number of 1.5×10^4. In particular, the laser cooling method of Eu is quite different from the standard laser cooling method since optical leak probabilities for the strong $J \rightarrow J+1$ transition is extraordinarily large. Considering the large optical leak, we proposed a new laser cooling scheme for Eu atoms. We started with a yellow-MOT that capture and cool optically pumped metastable Eu atoms. We have employed simultaneous MOT for the metastable and ground-state atoms. The trapped metastable atoms are successively pumped back to the ground state and then continuously loaded to the narrow-line MOT, where up to 4.7×10^7 atoms are captured.

Then we loaded the cold atoms to an optical dipole trap operating at a wavelength of 1550 nm for evaporative cooling, resulting in almost pure condensates of ^{151}Eu with 1.5×10^4 atoms. The effect of dipole-dipole interaction in the BEC was observed as the deformation of the expanding Eu condensate; the shape of the BEC after free expansion strongly depends on the orientation of the atomic dipole moments. By comparing the deformation of the condensate to the numerical simulation, I extracted an s-wave scattering length of $a_s = 135\,a_B$. In addition, I found a Feshbach resonance at a magnetic field of 1.3 G, and the shape of the condensate deformed in the vicinity of the resonance, which suggests a change of the s-wave scattering length.

8.2 Possible improvement for producing a BEC

We now can investigate properties of Eu BEC. However, the number of condensed atom is a bit small. Increasing number of atoms will lead to better signal-to-noise ratio. The number of condensed atom may be increased in the following method:

optical pumping with adiabatic passage process The optical pumping efficiency from the ground state to $a^{10}\mathrm{D}_{13/2}$ metastable state is estimated as $\sim$ 19 %. The low efficiency is due to spontaneous decay from $y^8\mathrm{P}_{9/2}$ to undesired metastable state. If one pump atoms from the ground state to $a^{10}\mathrm{D}_{11/2}$ metastable state with adiabatic passage process by using the 460 nm and 1204 nm laser light, loading rate to the red-MOT will increased by about 4 times.

introduce scanning ODT system Low loading efficiency from red-MOT to the horizontal ODT may be due to size mismatch between the horizontal ODT bean and red-MOT. Introducing tunable trapping volume system using an AOM may increase loading efficiency to the horizontal ODT.

8.3 Future task

Feshbach spectroscopy

Feshbach spectroscopy for Eu atom is now starting. If the Feshbach spectrum of Eu is sparse and not chaotic as expected by the theory, one may be able to determine molecular potential by comparing resonance positions with multichannel scattering calculations [90, 94]. The result can be used to determine the s-wave scattering length precisely for all combination of the total spin. These values are essential for spinor dipolar BEC experiment. Moreover, the molecular potential may be useful for searching weakly bound state available for microwave-induced Feshbach resonance, which we planed to use for exploring rich ground-state phases of dipolar BEC under ultra-low magnetic field.

Ultra-low magnetic field

Magnetic field control is crucial for exploring rich ground-state phases of dipolar BEC under ultra-low magnetic field. In roughly, Zeeman energy induced by external magnetic field must be smaller than the dipolar interaction energy, which correspond to a magnetic field of $10 \sim 100\,\mu$G. However, our BEC experiment is conducted in a metal chamber, where such a precise magnetic field control is nearly impossible. In future experiment, we will produce a BEC in a glass cell surrounded by magnetic shields made of permalloy.

Bibliography

[1] M. H. Anderson, J. R. Ensher, M. R. Matthews, C. E. Wieman, and E. A. Cornell, "Observation of Bose-Einstein condensation in a dilute atomic vapor," *Science*, vol. 269, no. 5221, pp. 198–201, 1995. [Online]. Available: https://science.sciencemag.org/content/269/5221/198

[2] K. B. Davis, M. O. Mewes, M. R. Andrews, N. J. van Druten, D. S. Durfee, D. M. Kurn, and W. Ketterle, "Bose-Einstein condensation in a gas of sodium atoms," *Phys. Rev. Lett.*, vol. 75, pp. 3969–3973, Nov 1995. [Online]. Available: https://link.aps.org/doi/10.1103/PhysRevLett.75.3969

[3] M. Egorov, B. Opanchuk, P. Drummond, B. V. Hall, P. Hannaford, and A. I. Sidorov, "Measurement of s-wave scattering lengths in a two-component Bose-Einstein condensate," *Phys. Rev. A*, vol. 87, p. 053614, May 2013. [Online]. Available: https://link.aps.org/doi/10.1103/PhysRevA.87.053614

[4] A. Griesmaier, J. Stuhler, T. Koch, M. Fattori, T. Pfau, and S. Giovanazzi, "Comparing contact and dipolar interactions in a Bose-Einstein condensate," *Phys. Rev. Lett.*, vol. 97, p. 250402, Dec 2006. [Online]. Available: https://link.aps.org/doi/10.1103/PhysRevLett.97.250402

[5] A. Frisch, "Dipolar quantum gases of erbium," Ph.D. dissertation, Physics of the University of Innsbruck, 2014.

[6] Y. Tang, A. Sykes, N. Q. Burdick, J. L. Bohn, and B. L. Lev, "s-wave scattering lengths of the strongly dipolar bosons ^{162}Dy and ^{164}Dy," *Phys. Rev. A*, vol. 92, p. 022703, Aug 2015. [Online]. Available: https://link.aps.org/doi/10.1103/PhysRevA.92.022703

[7] A. Griesmaier, J. Werner, S. Hensler, J. Stuhler, and T. Pfau, "Bose-Einstein condensation of chromium," *Phys. Rev. Lett.*, vol. 94, p. 160401, Apr 2005. [Online]. Available: https://link.aps.org/doi/10.1103/PhysRevLett.94.160401

[8] T. Lahaye, T. Koch, B. Fröhlich, M. Fattori, J. Metz, A. Griesmaier, S. Giovanazzi, and T. Pfau, "Strong dipolar effects in a quantum ferrofluid," *Nature*, vol. 448, no. 7154, pp. 672–675, Aug 2007. [Online]. Available: https://doi.org/10.1038/nature06036

[9] T. Lahaye, J. Metz, B. Fröhlich, T. Koch, M. Meister, A. Griesmaier, T. Pfau, H. Saito, Y. Kawaguchi, and M. Ueda, "d-wave collapse and explosion of a dipolar Bose-Einstein condensate," *Phys. Rev. Lett.*, vol. 101, p. 080401, Aug 2008. [Online]. Available: https://link.aps.org/doi/10.1103/PhysRevLett.101.080401

[10] M. Lu, N. Q. Burdick, S. H. Youn, and B. L. Lev, "Strongly dipolar Bose-Einstein condensate of dysprosium," *Phys. Rev. Lett.*, vol. 107, p. 190401, Oct 2011. [Online]. Available: https://link.aps.org/doi/10.1103/PhysRevLett.107.190401

[11] K. Aikawa, A. Frisch, M. Mark, S. Baier, A. Rietzler, R. Grimm, and F. Ferlaino, "Bose-Einstein condensation of erbium," *Phys. Rev. Lett.*, vol. 108, p. 210401, May 2012. [Online]. Available: https://link.aps.org/doi/10.1103/PhysRevLett.108.210401

[12] I. Ferrier-Barbut, H. Kadau, M. Schmitt, M. Wenzel, and T. Pfau, "Observation of quantum droplets in a strongly dipolar Bose gas," *Phys. Rev. Lett.*, vol. 116, p. 215301, May 2016. [Online]. Available: https://link.aps.org/doi/10.1103/PhysRevLett.116.215301

[13] L. Chomaz, S. Baier, D. Petter, M. J. Mark, F. Wächtler, L. Santos, and F. Ferlaino, "Quantum-fluctuation-driven crossover from a dilute Bose-Einstein condensate to a macrodroplet in a dipolar quantum fluid," *Phys. Rev. X*, vol. 6, p. 041039, Nov 2016. [Online]. Available: https://link.aps.org/doi/10.1103/PhysRevX.6.041039

[14] L. Tanzi, E. Lucioni, F. Famà, J. Catani, A. Fioretti, C. Gabbanini, R. N. Bisset, L. Santos, and G. Modugno, "Observation of a dipolar quantum gas with metastable supersolid properties," *Phys. Rev. Lett.*, vol. 122, p. 130405, Apr 2019. [Online]. Available: https://link.aps.org/doi/10.1103/PhysRevLett.122.130405

[15] D. Y. Kim and M. H. W. Chan, "Absence of supersolidity in solid helium in porous vycor glass," *Phys. Rev. Lett.*, vol. 109, p. 155301, Oct 2012. [Online]. Available: https://link.aps.org/doi/10.1103/PhysRevLett.109.155301

[16] F. Böttcher, J.-N. Schmidt, J. Hertkorn, K. S. H. Ng, S. D. Graham, M. Guo, T. Langen, and T. Pfau, "New states of matter with fine-tuned interactions: quantum droplets and dipolar supersolids," *Reports on Progress in Physics*, vol. 84, no. 1, p. 012403, jan 2021. [Online]. Available: https://doi.org/10.1088/1361-6633/abc9ab

[17] Y. Kawaguchi, H. Saito, and M. Ueda, "Spontaneous circulation in ground-state spinor dipolar Bose-Einstein condensates," *Phys. Rev. Lett.*, vol. 97, p. 130404, Sep 2006. [Online]. Available: https://link.aps.org/doi/10.1103/PhysRevLett.97.130404

[18] S. Yi and H. Pu, "Spontaneous spin textures in dipolar spinor condensates," *Phys. Rev. Lett.*, vol. 97, p. 020401, Jul 2006. [Online]. Available: https://link.aps.org/doi/10.1103/PhysRevLett.97.020401

[19] M. Takahashi, S. Ghosh, T. Mizushima, and K. Machida, "Spinor dipolar Bose-Einstein condensates: Classical spin approach," *Phys. Rev. Lett.*, vol. 98, p. 260403, Jun 2007. [Online]. Available: https://link.aps.org/doi/10.1103/PhysRevLett.98.260403

[20] D. M. Stamper-Kurn, M. R. Andrews, A. P. Chikkatur, S. Inouye, H.-J. Miesner, J. Stenger, and W. Ketterle, "Optical confinement of a bose-einstein condensate," *Phys. Rev. Lett.*, vol. 80, pp. 2027–2030, Mar 1998. [Online]. Available: https://link.aps.org/doi/10.1103/PhysRevLett.80.2027

[21] Y. Kawaguchi and M. Ueda, "Spinor bose–einstein condensates," *Physics Reports*, vol. 520, no. 5, pp. 253–381, 2012, spinor Bose–Einstein condensates. [Online]. Available: https://www.sciencedirect.com/science/article/pii/S0370157312002098

[22] L. Santos and T. Pfau, "Spin-3 chromium bose-einstein condensates," *Phys. Rev. Lett.*, vol. 96, p. 190404, May 2006. [Online]. Available: https://link.aps.org/doi/10.1103/PhysRevLett.96.190404

[23] M. Vengalattore, S. R. Leslie, J. Guzman, and D. M. Stamper-Kurn, "Spontaneously modulated spin textures in a dipolar spinor Bose-Einstein condensate," *Phys. Rev. Lett.*, vol. 100, p. 170403, May 2008. [Online]. Available: https://link.aps.org/doi/10.1103/PhysRevLett.100.170403

[24] Y. Eto, H. Saito, and T. Hirano, "Observation of dipole-induced spin texture in an ^{87}Rb Bose-Einstein condensate," *Phys. Rev. Lett.*, vol. 112, p. 185301, May 2014. [Online]. Available: https://link.aps.org/doi/10.1103/PhysRevLett.112.185301

[25] S. Lepoutre, K. Kechadi, B. Naylor, B. Zhu, L. Gabardos, L. Isaev, P. Pedri, A. M. Rey, L. Vernac, and B. Laburthe-Tolra, "Spin mixing and protection of ferromagnetism in a spinor dipolar condensate," *Phys. Rev. A*, vol. 97, p. 023610, Feb 2018. [Online]. Available: https://link.aps.org/doi/10.1103/PhysRevA.97.023610

[26] S. Lepoutre, L. Gabardos, K. Kechadi, P. Pedri, O. Gorceix, E. Maréchal, L. Vernac, and B. Laburthe-Tolra, "Collective spin modes of a trapped quantum ferrofluid," *Phys. Rev. Lett.*, vol. 121, p. 013201, Jul 2018. [Online]. Available: https://link.aps.org/doi/10.1103/PhysRevLett.121.013201

[27] S. Baier, M. J. Mark, D. Petter, K. Aikawa, L. Chomaz, Z. Cai, M. Baranov, P. Zoller, and F. Ferlaino, "Extended Bose-Hubbard models with ultracold magnetic atoms," *Science*, vol. 352, no. 6282, pp. 201–205, 2016. [Online]. Available: https://science.sciencemag.org/content/352/6282/201

[28] L. Gabardos, B. Zhu, S. Lepoutre, A. M. Rey, B. Laburthe-Tolra, and L. Vernac, "Relaxation of the collective magnetization of a dense 3d array of interacting dipolar $s = 3$ atoms," *Phys. Rev. Lett.*, vol. 125, p. 143401, Sep 2020. [Online]. Available: https://link.aps.org/doi/10.1103/PhysRevLett.125.143401

[29] D. J. Papoular, G. V. Shlyapnikov, and J. Dalibard, "Microwave-induced fano-feshbach resonances," *Phys. Rev. A*, vol. 81, p. 041603, Apr 2010. [Online]. Available: https://link.aps.org/doi/10.1103/PhysRevA.81.041603

[30] T. Maier, H. Kadau, M. Schmitt, M. Wenzel, I. Ferrier-Barbut, T. Pfau, A. Frisch, S. Baier, K. Aikawa, L. Chomaz, M. J. Mark, F. Ferlaino, C. Makrides, E. Tiesinga, A. Petrov, and S. Kotochigova, "Emergence of chaotic scattering in ultracold er and dy," *Phys. Rev. X*, vol. 5, p. 041029, Nov 2015. [Online]. Available: https://link.aps.org/doi/10.1103/PhysRevX.5.041029

[31] A. Frisch, M. Mark, K. Aikawa, F. Ferlaino, J. L. Bohn, C. Makrides, A. Petrov, and S. Kotochigova, "Quantum chaos in ultracold collisions of gas-phase erbium atoms," *Nature*, vol. 507, no. 7493, pp. 475–479, Mar 2014. [Online]. Available: https://doi.org/10.1038/nature13137

[32] T. Maier, I. Ferrier-Barbut, H. Kadau, M. Schmitt, M. Wenzel, C. Wink, T. Pfau, K. Jachymski, and P. S. Julienne, "Broad universal feshbach resonances in the chaotic spectrum of dysprosium atoms," *Phys. Rev. A*, vol. 92, p. 060702, Dec 2015. [Online]. Available: https://link.aps.org/doi/10.1103/PhysRevA.92.060702

[33] V. A. Khlebnikov, D. A. Pershin, V. V. Tsyganok, E. T. Davletov, I. S. Cojocaru, E. S. Fedorova, A. A. Buchachenko, and A. V. Akimov, "Random to chaotic statistic transformation in low-field fano-feshbach resonances of cold thulium atoms," *Phys. Rev. Lett.*, vol. 123, p. 213402, Nov 2019. [Online]. Available: https://link.aps.org/doi/10.1103/PhysRevLett.123.213402

[34] K. Zaremba-Kopczyk, P. S. Żuchowski, and M. Tomza, "Magnetically tunable feshbach resonances in ultracold gases of europium atoms and mixtures of europium and alkali-metal atoms," *Phys. Rev. A*, vol. 98, p. 032704, Sep 2018. [Online]. Available: https://link.aps.org/doi/10.1103/PhysRevA.98.032704

[35] J. R. de Laeter, J. K. Böhlke, P. D. Bièvre, H. Hidaka, H. S. Peiser, K. J. R. Rosman, and P. D. P. Taylor, "Atomic weights of the elements. review 2000 (iupac technical report)," *Pure and Applied Chemistry*, vol. 75, no. 6, pp. 683 – 800, 01 Jan. 2003. [Online]. Available: https://www.degruyter.com/view/journals/pac/75/6/article-p683.xml

[36] N. Casali, S. S. Nagorny, F. Orio, L. Pattavina, J. W. Beeman, F. Bellini, L. Cardani, I. Dafinei, S. D. Domizio, M. L. D. Vacri, L. Gironi, M. B. Kosmyna, B. P. Nazarenko, S. Nisi, G. Pessina, G. Piperno, S. Pirro, C. Rusconi, A. N. Shekhovtsov, C. Tomei, and M. Vignati, "Discovery of the151eu α decay," *Journal of Physics G: Nuclear and Particle Physics*, vol. 41, no. 7, p. 075101, apr 2014. [Online]. Available: https://doi.org/10.1088%2F0954-3899%2F41%2F7%2F075101

[37] G. Audi, O. Bersillon, J. Blachot, and A. Wapstra, "The nubase evaluation of nuclear and decay properties," *Nuclear Physics A*, vol. 729, no. 1, pp. 3 – 128, 2003, the 2003 NUBASE and Atomic Mass Evaluations. [Online]. Available: http://www.sciencedirect.com/science/article/pii/S0375947403018074

[38] W.-G. Jin, T. Endo, T. Wakui, H. Uematsu, T. Minowa, and H. Katsuragawa, "Measurements of the hyperfine structure and δf=+2 transitions in eu i by high-resolution diode-laser spectroscopy," *Journal of the Physical Society of Japan*, vol. 71, no. 8, pp. 1905–1909, 2002. [Online]. Available: https://doi.org/10.1143/JPSJ.71.1905

[39] T. M. Hanna, E. Tiesinga, and P. S. Julienne, "Creation and manipulation of feshbach resonances with radiofrequency radiation," *New Journal of Physics*, vol. 12,

no. 8, p. 083031, aug 2010. [Online]. Available: https://doi.org/10.1088/1367-2630/12/8/083031

[40] J. Miao, J. Hostetter, G. Stratis, and M. Saffman, "Magneto-optical trapping of holmium atoms," *Phys. Rev. A*, vol. 89, p. 041401, Apr 2014. [Online]. Available: https://link.aps.org/doi/10.1103/PhysRevA.89.041401

[41] D. Sesko, T. Walker, C. Monroe, A. Gallagher, and C. Wieman, "Collisional losses from a light-force atom trap," *Phys. Rev. Lett.*, vol. 63, pp. 961–964, Aug 1989. [Online]. Available: https://link.aps.org/doi/10.1103/PhysRevLett.63.961

[42] J. A. Dean, "Lange'shandbookofchemistry (15th edition)," 1999.

[43] C. B. Alcock, V. P. Itkin, and M. K. Horrigan, "Vapour pressure equations for the metallic elements: 298–2500k," *Canadian Metallurgical Quarterly*, vol. 23, no. 3, pp. 309–313, 1984. [Online]. Available: https://doi.org/10.1179/cmq.1984.23.3.309

[44] Y. Miyazawa, R. Inoue, K. Nishida, T. Hosoya, and M. Kozuma, "Measuring the branching ratios from the y8p9/2 state to metastable states in europium," *Optics Communications*, vol. 392, pp. 171–174, 2017. [Online]. Available: https://www.sciencedirect.com/science/article/pii/S0030401817300858

[45] R. Inoue, Y. Miyazawa, and M. Kozuma, "Magneto-optical trapping of optically pumped metastable europium," *Phys. Rev. A*, vol. 97, p. 061607, Jun 2018. [Online]. Available: https://link.aps.org/doi/10.1103/PhysRevA.97.061607

[46] T. Kuwamoto, K. Honda, Y. Takahashi, and T. Yabuzaki, "Magneto-optical trapping of yb atoms using an intercombination transition," *Phys. Rev. A*, vol. 60, pp. R745–R748, Aug 1999. [Online]. Available: https://link.aps.org/doi/10.1103/PhysRevA.60.R745

[47] T. Maier, H. Kadau, M. Schmitt, A. Griesmaier, and T. Pfau, "Narrow-line magneto-optical trap for dysprosium atoms," *Opt. Lett.*, vol. 39, no. 11, pp. 3138–3141, Jun 2014. [Online]. Available: http://ol.osa.org/abstract.cfm?URI=ol-39-11-3138

[48] A. Frisch, K. Aikawa, M. Mark, A. Rietzler, J. Schindler, E. Zupanič, R. Grimm, and F. Ferlaino, "Narrow-line magneto-optical trap for erbium," *Phys. Rev. A*, vol. 85, p. 051401, May 2012. [Online]. Available: https://link.aps.org/doi/10.1103/PhysRevA.85.051401

[49] D. D. Sukachev, E. S. Kalganova, A. V. Sokolov, S. A. Fedorov, G. A. Vishnyakova, A. V. Akimov, N. N. Kolachevsky, and V. N. Sorokin, "Secondary laser cooling and capturing of thulium atoms in traps," *Quantum Electron.*, vol. 44, no. 6, pp. 515–520, jun 2014. [Online]. Available: https://doi.org/10.1070%2Fqe2014v044n06abeh015392

[50] R. Z. W. C. Martin and L. Hagan, *Atomic Energy Levels—The Rare-Earth Elements, National Standard Reference DataSeries Vol. 60.* National Bureau of Standards, 1978. [Online]. Available: https://physics.nist.gov/PhysRefData/Handbook/Tables/europiumtable5.htm

[51] E. A. D. Hartog, M. E. Wickliffe, and J. E. Lawler, "Radiative lifetimes of eu i , ii , and iii and transition probabilities of eu i," *The Astrophysical Journal Supplement Series*, vol. 141, no. 1, pp. 255–265, jul 2002. [Online]. Available: https://doi.org/10.1086/340039

[52] B. Fechner, R.-H. Rinkleff, and A. Steudel, "Radiative lifetimes of levels of the configuration 4f7 (8s) 6s 6p in eu i," *Zeitschrift für Physik D Atoms, Molecules and Clusters*, vol. 6, no. 1, pp. 31–34, Mar 1987. [Online]. Available: https://doi.org/10.1007/BF01436994

[53] S. H. Youn, M. Lu, U. Ray, and B. L. Lev, "Dysprosium magneto-optical traps," *Phys. Rev. A*, vol. 82, p. 043425, Oct 2010. [Online]. Available: https://link.aps.org/doi/10.1103/PhysRevA.82.043425

[54] J. J. McClelland and J. L. Hanssen, "Laser cooling without repumping: A magneto-optical trap for erbium atoms," *Phys. Rev. Lett.*, vol. 96, p. 143005, Apr 2006. [Online]. Available: https://link.aps.org/doi/10.1103/PhysRevLett.96.143005

[55] D. Sukachev, A. Sokolov, K. Chebakov, A. Akimov, S. Kanorsky, N. Kolachevsky, and V. Sorokin, "Magneto-optical trap for thulium atoms," *Phys. Rev. A*, vol. 82, p. 011405, Jul 2010. [Online]. Available: https://link.aps.org/doi/10.1103/PhysRevA.82.011405

[56] K. Honda, Y. Takahashi, T. Kuwamoto, M. Fujimoto, K. Toyoda, K. Ishikawa, and T. Yabuzaki, "Magneto-optical trapping of yb atoms and a limit on the branching ratio of the $^1P_1$ state," *Phys. Rev. A*, vol. 59, pp. R934–R937, Feb 1999. [Online]. Available: https://link.aps.org/doi/10.1103/PhysRevA.59.R934

[57] M. Okano, "Simultaneous magneto-optical trapping of lithium and ytterbium atoms: Towards production of ultracold polar molecules," Ph.D. dissertation, Kyoto University, 2009.

[58] B. Furmann, J. Ruczkowski, M. Chomski, M. Suski, S. Wilman, and D. Stefańska, "Landé gj factors of the electronic levels of the europium atom," *Journal of Quantitative Spectroscopy and Radiative Transfer*, vol. 255, p. 107258, 2020. [Online]. Available: https://www.sciencedirect.com/science/article/pii/S0022407320306543

[59] H. Matsui, Y. Miyazawa, R. Inoue, and M. Kozuma, "Magnetic trap of metastable europium atoms," 2021.

[60] D. A. Steck, "'rubidium 87 d line data," available online at http://steck.us/alkalidata (revision 2.2.1,21 November 2019). [Online]. Available: https://steck.us/alkalidata/rubidium87numbers.pdf

[61] G. J. Zaal, W. Hogervorst, E. R. Eliel, K. A. H. van Leeuwen, and J. Blok, "A high resolution study of the transitions 4f76s2 → 4f76s6p in the eu i-spectrum," *Z. Phys. A*, vol. 290, no. 4, pp. 339–344, Dec 1979. [Online]. Available: https://doi.org/10.1007/BF01408393

[62] T. Ogata, "Yuropiumu genshi kitai no bo-su gyousyuku ni muketa ze-man gensokuki no koukourituka," Master's thesis, Tokyo Institute of Technology, 2018.

[63] R. Grimm, M. Weidemüller, and Y. B. Ovchinnikov, "Optical dipole traps for neutral atoms," ser. Advances In Atomic, Molecular, and Optical Physics, B. Bederson and H. Walther, Eds. Academic Press, 2000, vol. 42, pp. 95–170. [Online]. Available: https://www.sciencedirect.com/science/article/pii/S1049250X0860186X

[64] T. Arpornthip, C. A. Sackett, and K. J. Hughes, "Vacuum-pressure measurement using a magneto-optical trap," *Phys. Rev. A*, vol. 85, p. 033420, Mar 2012. [Online]. Available: https://link.aps.org/doi/10.1103/PhysRevA.85.033420

[65] R. W. P. Drever, J. L. Hall, F. V. Kowalski, J. Hough, G. M. Ford, A. J. Munley, and H. Ward, "Laser phase and frequency stabilization using an optical resonator," *Applied Physics B*, vol. 31, no. 2, pp. 97–105, Jun 1983. [Online]. Available: https://doi.org/10.1007/BF00702605

[66] D. Dreon, L. A. Sidorenkov, C. Bouazza, W. Maineult, J. Dalibard, and S. Nascimbene, "Optical cooling and trapping of highly magnetic atoms: the benefits of a spontaneous spin polarization," *Journal of Physics B: Atomic, Molecular and Optical Physics*, vol. 50, no. 6, p. 065005, mar 2017. [Online]. Available: https://doi.org/10.1088/1361-6455/aa5db5

[67] V. V. Tsyganok, D. A. Pershin, E. T. Davletov, V. A. Khlebnikov, and A. V. Akimov, "Scalar, tensor, and vector polarizability of tm atoms in a 532-nm dipole trap," *Phys. Rev. A*, vol. 100, p. 042502, Oct 2019. [Online]. Available: https://link.aps.org/doi/10.1103/PhysRevA.100.042502

[68] J. H. Becher, S. Baier, K. Aikawa, M. Lepers, J.-F. Wyart, O. Dulieu, and F. Ferlaino, "Anisotropic polarizability of erbium atoms," *Phys. Rev. A*, vol. 97, p. 012509, Jan 2018. [Online]. Available: https://link.aps.org/doi/10.1103/PhysRevA.97.012509

[69] M. Lepers, J.-F. Wyart, and O. Dulieu, "Anisotropic optical trapping of ultracold erbium atoms," *Phys. Rev. A*, vol. 89, p. 022505, Feb 2014. [Online]. Available: https://link.aps.org/doi/10.1103/PhysRevA.89.022505

[70] D. Sukachev, S. Fedorov, I. Tolstikhina, D. Tregubov, E. Kalganova, G. Vishnyakova, A. Golovizin, N. Kolachevsky, K. Khabarova, and V. Sorokin, "Inner-shell magnetic dipole transition in tm atoms: A candidate for optical lattice clocks," *Phys. Rev. A*, vol. 94, p. 022512, Aug 2016. [Online]. Available: https://link.aps.org/doi/10.1103/PhysRevA.94.022512

[71] S. Fan, Q. Wang, X. Shang, Y. Tian, and Z. Dai, "Experimental branching fractions, transition probabilities and oscillator strengths in eu i," *Journal of Physics B: Atomic, Molecular and Optical Physics*, vol. 47, no. 21, p. 215004, oct 2014. [Online]. Available: https://doi.org/10.1088/0953-4075/47/21/215004

[72] H. Li, J.-F. Wyart, O. Dulieu, S. Nascimbène, and M. Lepers, "Optical trapping of ultracold dysprosium atoms: transition probabilities, dynamic dipole polarizabilities and van der WaalsC6coefficients," *Journal of Physics B: Atomic, Molecular and Optical Physics*, vol. 50, no. 1, p. 014005, dec 2016. [Online]. Available: https://doi.org/10.1088/1361-6455/50/1/014005

[73] Y. Takasu, K. Maki, K. Komori, T. Takano, K. Honda, M. Kumakura, T. Yabuzaki, and Y. Takahashi, "Spin-singlet Bose-Einstein condensation of two-electron atoms," *Phys. Rev. Lett.*, vol. 91, p. 040404, Jul 2003. [Online]. Available: https://link.aps.org/doi/10.1103/PhysRevLett.91.040404

[74] S. Baier, "An optical dipole trap for erbiumwith tunable geometry," Master's thesis, Mathematics, Computer Science and Physicsof the University of Innsbruck, 2012. [Online]. Available: http://www.erbium.at/FF/wp-content/uploads/2015/10/master_simon_baier.pdf

[75] C. Politi, "Optical dipole trap for an erbium anddysprosium mixture," Master's thesis, Università di Pisa, 2017. [Online]. Available: http://www.erbium.at/FF/wp-content/uploads/2017/11/Master_Claudia_Politi.pdf

[76] V. V. Tsyganok, V. A. Khlebnikov, E. S. Kalganova, D. A. Pershin, E. T. Davletov, I. S. Cojocaru, I. A. Luchnikov, A. V. Berezutskii, V. S. Bushmakin, V. N. Sorokin, and A. V. Akimov, "Polarized cold cloud of thulium atom," *Journal of Physics B: Atomic, Molecular and Optical Physics*, vol. 51, no. 16, p. 165001, jul 2018. [Online]. Available: https://doi.org/10.1088/1361-6455/aad445

[77] T. Chalopin, V. Makhalov, C. Bouazza, A. Evrard, A. Barker, M. Lepers, J.-F. m. c. Wyart, O. Dulieu, J. Dalibard, R. Lopes, and S. Nascimbene, "Anisotropic light shift and magic polarization of the intercombination line of dysprosium atoms in a far-detuned dipole trap," *Phys. Rev. A*, vol. 98, p. 040502, Oct 2018. [Online]. Available: https://link.aps.org/doi/10.1103/PhysRevA.98.040502

[78] Y. Castin, "Bose-Einstein condensates in atomic gases: Simple theoretical results," in *Coherent atomic matter waves*, R. Kaiser, C. Westbrook, and F. David, Eds. Berlin, Heidelberg: Springer Berlin Heidelberg, 2001, pp. 1–136. [Online]. Available: https://arxiv.org/abs/cond-mat/0105058

[79] S. Giorgini, L. P. Pitaevskii, and S. Stringari, "Condensate fraction and critical temperature of a trapped interacting Bose gas," *Phys. Rev. A*, vol. 54, pp. R4633–R4636, Dec 1996. [Online]. Available: https://link.aps.org/doi/10.1103/PhysRevA.54.R4633

[80] A. J. Olson, R. J. Niffenegger, and Y. P. Chen, "Optimizing the efficiency of evaporative cooling in optical dipole traps," *Phys. Rev. A*, vol. 87, p. 053613, May 2013. [Online]. Available: https://link.aps.org/doi/10.1103/PhysRevA.87.053613

[81] J. Söding, D. Guéry-Odelin, P. Desbiolles, F. Chevy, H. Inamori, and J. Dalibard, "Three-body decay of a rubidium Bose–Einstein condensate," *Applied Physics B*, vol. 69, no. 4, pp. 257–261, Oct 1999. [Online]. Available: https://doi.org/10.1007/s003400050805

[82] J. Stuhler, A. Griesmaier, T. Koch, M. Fattori, T. Pfau, S. Giovanazzi, P. Pedri, and L. Santos, "Observation of dipole-dipole interaction in a degenerate quantum gas," *Phys. Rev. Lett.*, vol. 95, p. 150406, Oct 2005. [Online]. Available: https://link.aps.org/doi/10.1103/PhysRevLett.95.150406

[83] S. Giovanazzi, P. Pedri, L. Santos, A. Griesmaier, M. Fattori, T. Koch, J. Stuhler, and T. Pfau, "Expansion dynamics of a dipolar Bose-Einstein condensate," *Phys. Rev. A*, vol. 74, p. 013621, Jul 2006. [Online]. Available: https://link.aps.org/doi/10.1103/PhysRevA.74.013621

[84] A. R. Griesmaier, "Dipole-dipole interactionin a degenerate quantum gas Bose-Einstein condensationof chromium atoms," Ph.D. dissertation, 5th Institute of Physics, University of Stuttgart, 2006. [Online]. Available: https://www.pi5.uni-stuttgart.de/documents/abgeschlossene-arbeiten/2006-Griesmaier-Axel-Dipole-dipole-interaction-in-a-degenerate-quantum-gas-Bose-Einstein-condensation-of-chromium-atoms-PhD.pdf

[85] B. Fröhlich, "Strong dipolar effects in a chromium Bose-Einstein condensate," Ph.D. dissertation, 5th Institute of Physics, University of Stuttgart, 2007. [Online]. Available: https://www.pi5.uni-stuttgart.de/documents/abgeschlossene-arbeiten/2007-Froehlich-Bernd-Strong-Dipolar-Effects-in-a-Chromium-Bose-Einstein-Condensate-Diplom.pdf

[86] A. Griesmaier, "Generation of a dipolar Bose-Einstein condensate," *Journal of Physics B: Atomic, Molecular and Optical Physics*, vol. 40, no. 14, pp. R91–R134, jul 2007. [Online]. Available: https://doi.org/10.1088/0953-4075/40/14/r01

[87] T. Lahaye, C. Menotti, L. Santos, M. Lewenstein, and T. Pfau, "The physics of dipolar bosonic quantum gases," *Reports on Progress in Physics*, vol. 72, no. 12, p. 126401, nov 2009. [Online]. Available: https://doi.org/10.1088/0034-4885/72/12/126401

[88] D. H. J. O'Dell, S. Giovanazzi, and C. Eberlein, "Exact hydrodynamics of a trapped dipolar Bose-Einstein condensate," *Phys. Rev. Lett.*, vol. 92, p. 250401, Jun 2004. [Online]. Available: https://link.aps.org/doi/10.1103/PhysRevLett.92.250401

[89] Y. Castin and R. Dum, "Bose-Einstein condensates in time dependent traps," *Phys. Rev. Lett.*, vol. 77, pp. 5315–5319, Dec 1996. [Online]. Available: https://link.aps.org/doi/10.1103/PhysRevLett.77.5315

[90] J. Werner, A. Griesmaier, S. Hensler, J. Stuhler, T. Pfau, A. Simoni, and E. Tiesinga, "Observation of feshbach resonances in an ultracold gas of ^{52}Cr," *Phys. Rev. Lett.*, vol. 94, p. 183201, May 2005. [Online]. Available: https://link.aps.org/doi/10.1103/PhysRevLett.94.183201

[91] C. Chin, R. Grimm, P. Julienne, and E. Tiesinga, "Feshbach resonances in ultracold gases," *Rev. Mod. Phys.*, vol. 82, pp. 1225–1286, Apr 2010. [Online]. Available: https://link.aps.org/doi/10.1103/RevModPhys.82.1225

[92] K. Baumann, N. Q. Burdick, M. Lu, and B. L. Lev, "Observation of low-field fano-feshbach resonances in ultracold gases of dysprosium," *Phys. Rev. A*, vol. 89, p. 020701, Feb 2014. [Online]. Available: https://link.aps.org/doi/10.1103/PhysRevA.89.020701

[93] V. A. Khlebnikov, V. V. Tsyganok, D. A. Pershin, E. T. Davletov, E. Kuznetsova, and A. V. Akimov, "Characterizing the temperature dependence of fano-feshbach resonances of ultracold polarized thulium," *Phys. Rev. A*, vol. 103, p. 023306, Feb 2021. [Online]. Available: https://link.aps.org/doi/10.1103/PhysRevA.103.023306

[94] J. Werner, "Observation of feshbach resonances in an ultracold gas of ^{52}Cr," Ph.D. dissertation, Von der Fakultät Mathematik und Physik der Universität Stuttgart, 2006. [Online]. Available: https://elib.uni-stuttgart.de/bitstream/11682/4799/1/diss_final_online.pdf

Acknowledgements

First and foremost I would like to thank my advisor Prof. Mikio Kozuma. Since I started this research under his advice in my fourth year of undergraduate, he taught me all the theoretical and experimental aspects of ultracold atoms. During the seven years of research in this laboratory, he encouraged my research and allowed me to grow as a research scientist.

I would also like to express my gratitude to the members of the examination committee, Toshimasa Fujisawa, Hideto Kanamori, Yusuke Nishida, Kiyotaka Aikawa, and Mikio Kozuma, who dedicated their time and interest and provided helpful comments.

I acknowledge all the people who collaborated experimentally and theoretically in the realization of this project: Toshiyuki Hosoya, Kieiji Nishida, Takuya Ogata, Syunsuke Taga, Hiroki Matusi, Kenta Takanashi, Naoki Yoshikawa, Gyohei Nomura, Issyu Honda, Martin Miranda, Ryotaro Inoue and Mikio Kozuma.

Finally, this project would have not been possible without all the generous financial support. Everyday financial support for my Ph.D. course was provided by the Japan Society for Japan Society for the Promotion of Science.

Yuki Miyazawa